

On-chip black hole: Hawking radiation and curved spacetime in a superconducting quantum circuit with tunable couplers

Yun-Hao Shi,^{1, 2, *} Run-Qiu Yang,^{3, *} Zhongcheng Xiang,^{1, *} Zi-Yong Ge,⁴ Hao Li,^{1, 5} Yong-Yi Wang,^{1, 2} Kaixuan Huang,¹ Ye Tian,¹ Xiaohui Song,¹ Dongning Zheng,^{1, 2, 6, 7, †} Kai Xu,^{1, 2, 6, 7, ‡} Rong-Gen Cai,^{8, §} and Heng Fan^{1, 2, 6, 7, ¶}

¹ Institute of Physics, Chinese Academy of Sciences, Beijing 100190, China

² School of Physical Sciences, University of Chinese Academy of Sciences, Beijing 100190, China

³ Center for Joint Quantum Studies and Department of Physics,

School of Science, Tianjin University, Tianjin 300350, China

⁴ Theoretical Quantum Physics Laboratory, RIKEN Cluster for Pioneering Research, Wako-shi, Saitama 351-0198, Japan

⁵ School of Physics, Northwest University, Xi'an 710127, China

⁶ Beijing Academy of Quantum Information Sciences,
and CAS Center for Excellence in Topological Quantum Computation,

University of Chinese Academy of Sciences, Beijing 100190, China

⁷ Songshan Lake Materials Laboratory, Dongguan, Guangdong 523808, China

⁸ CAS Key Laboratory of Theoretical Physics, Institute of Theoretical Physics,
Chinese Academy of Sciences, Beijing 100190, China

Hawking radiation is one of quantum features of a black hole that can be understood as a quantum tunneling across the event horizon of the black hole, but it is quite difficult to directly observe the Hawking radiation of an astrophysical black hole. Remarkable experiments of analogue black holes on various platforms have been performed. However, due to the experimental difficulty of accurately constructing curved spacetime and precisely measuring the thermal spectrum, Hawking radiation and its quantum nature, such as entanglement, have not been adequately investigated. Based on the recent architecture breakthrough of tunable couplers for superconducting processors, we experimentally realize an analogue black hole using our new developed chip with a chain of 10 superconducting transmon qubits with interactions mediated by 9 transmon-type tunable couplers. By developing efficient techniques to engineer the couplings between qubits via tuning couplers, we achieve both the flat and curved spacetime backgrounds. The quantum walks of quasi-particle in the curved spacetime reflect the gravitational effect near the black hole, resulting in the behavior of Hawking radiation. By virtue of the state tomography measurement of all 7 qubits outside the analogue event horizon, we show that Hawking radiation can be verified. In addition, an entangled pair is prepared inside the horizon and the dynamics of entanglement in the curved spacetime is directly measured. Our results would stimulate more interests to explore the related features of black holes using programmable superconducting processor with tunable couplers.

Introduction.—In the classical picture, a particle falls into a black hole horizon and the horizon prevents the particle from turning back, then escape becomes impossible. However, taking into account quantum effect, the particle inside the black hole is doomed to gradually escape to the outside, leading to the Hawking radiation [1]. The problem is that direct observation of such a quantum effect of a real black hole is difficult in astrophysics. For a black hole with solar mass, the associated Hawking temperature is only $\sim 10^{-8}$ K and the corresponding radiation probability is astronomically small. Given by this, various analogue systems were proposed to simulate a black hole and its physical effects in laboratories [2]. Over the past years, the theory of Hawking radiation has been tested in experiments based on various platforms engineered with analogue black holes, such as using supersonic fluid [2–7], Bose-Einstein condensates [8–10], optical metamaterials and light [11–13], etc.

On the other hand, the developments of superconducting processor enable us to simulate various intriguing problems of many-body systems, molecules, and to achieve quantum computational supremacy [14–17].

However, constructing an analogue black hole on a superconducting chip is still a challenge, which requires wide-range tunable and site-dependent couplings between qubits to realize the curved spacetime [18]. Coincidentally, a recent architectural breakthrough of tunable couplers for superconducting circuit [19], which has been exploited to implement fast and high-fidelity two-qubit gates [20–22], offers an opportunity to achieve specific coupling distribution analogous to the curved spacetime. We develop such a superconducting processor integrated with a one-dimensional (1D) array of 10 qubits with interaction couplings controlled by 9 tunable couplers, see Fig. 1, which can realize both flat and curved spacetime backgrounds. The quantum walks of quasi-particle excitations of superconducting qubits are performed to simulate dynamics of particles in a black hole background, including dynamics of entangled pair inside the horizon. By using multiqubit state tomography, Hawking radiation is measured which is in agreement with theory prediction. This new constructed analogue black hole then facilitates further investigations of other related problems of black hole.

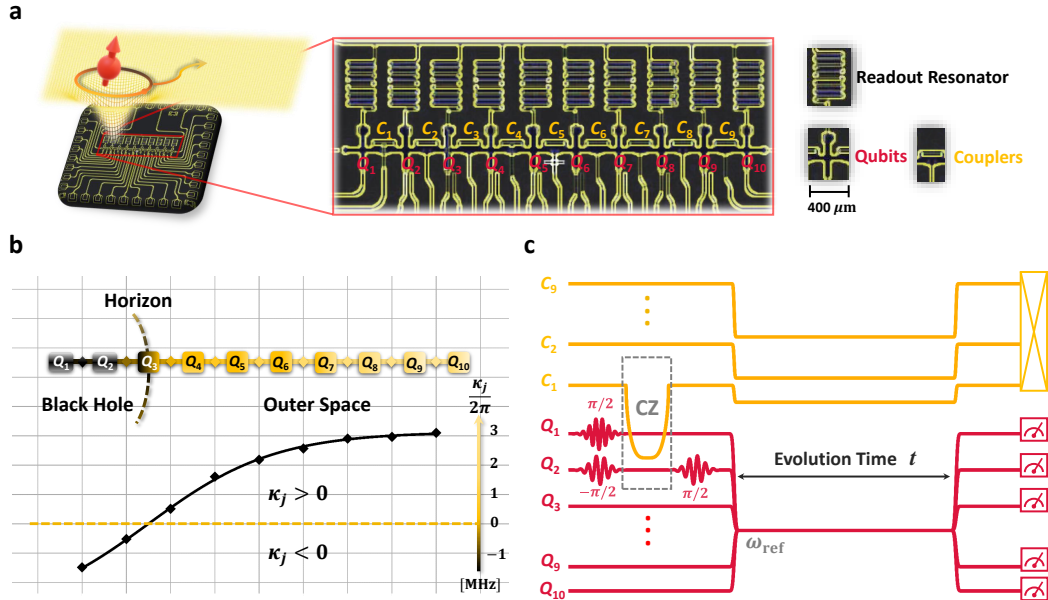


FIG. 1. **On-chip analogue black hole.** **a**, False-color image of superconducting processor and schematic analogue black hole. Ten transmon qubits, $Q_1 \sim Q_{10}$, shown as cross, are integrated along a chain with nearest-neighbor couplings. Each nearest-neighbor two qubits are coupled via a coupler, $C_1 \sim C_9$, realized by a transmon with only a flux bias line. All the transmons are frequency-tunable, but only qubit has XY control line and readout resonator. The schematic image represents the background of curved spacetime simulated by this superconducting chip. The red cartoon spin located at upper-left denotes the evolution of one quasi-particle that are initially in the black hole and the outward-going radiation. **b**, Schematic representation of the site-dependent effective coupling strengths κ_j . In the experiment, the coupling κ_j is designed according to Eq. (3). There is a boundary analogous to the event horizon of a black hole, where the coupling changes its sign at site Q_3 . Thus qubits Q_1 and Q_2 can be considered as the interior of black hole, Q_3 is at the horizon, and $Q_4 \sim Q_{10}$ are in the outside black hole. **c**, Experimental pulse sequence for observing dynamics of entanglement. The pulse sequences of frequency are presented for preparing an entangled pair on Q_1Q_2 , which are mediated by coupler C_1 , in the analogue black hole.

Model and setup.—Consider a general two-dimensional spacetime background with a fixed static metric $g_{\mu\nu}$, the metric in the Schwarzschild coordinates (t_s, x) reads $ds^2 = f(x)dt_s^2 - f^{-1}(x)dx^2$. To describe a black hole with nonzero temperature in 2-dimensional spacetime, we require that the function f has a root at $x = x_h$ with $f'(x_h) > 0$ and $f(x) > 0$ for $x > x_h$ standing for the exterior of the black hole, while $f(x) < 0$ for $x < x_h$ for the interior. The horizon of black hole then locates at $x = x_h$. For our purpose and experimental setups, we transform above metric into “advanced Eddington-Finkelstein coordinates” by the coordinates transformation $t = t_s + \int f^{-1}(x)dx$. In the coordinates $\{t, x\}$, the metric now becomes $ds^2 = f(x)dt^2 - 2dtdx$. A brief introduction on the differences between the “time-orthogonal coordinates” and “advanced Eddington-Finkelstein coordinates” can be found in our Supplementary Material.

To consider the effects of quantum matters in curved spacetime, we consider a Dirac field, of which the Dirac equation is written as [23, 24]

$$i\gamma^a e_{(a)}^\mu \partial_\mu \psi + \frac{i}{2} \gamma^a \frac{1}{\sqrt{-g}} \partial_\mu \left(\sqrt{-g} e_{(a)}^\mu \right) \psi - m\psi = 0, \quad (1)$$

where g is the determinate of $g_{\mu\nu}$, the vielbein $e_\mu^{(a)}$ sat-

isfies the orthonormal condition $e_\mu^{(a)} e_{(a)}^\nu = \delta_\mu^\nu$ and the γ -matrices in the two-dimensional case are chosen to be $\gamma = (\sigma_z, i\sigma_y)$. In the Eddington-Finkelstein coordinates $\{t, x\}$ and in the massless limit $m \rightarrow 0$, such a Dirac field can be quantized into a discrete XY lattice model with site-dependent hopping couplings. The effective Hamiltonian reads (see Supplementary and Ref. [18])

$$\frac{\hat{H}}{\hbar} = - \sum_j \kappa_j (\hat{\sigma}_j^+ \hat{\sigma}_{j+1}^- + \hat{\sigma}_j^- \hat{\sigma}_{j+1}^+) - \sum_j \mu_j \hat{\sigma}_j^+ \hat{\sigma}_j^-, \quad (2)$$

where \hbar is the reduced Planck constant (for convenience \hbar will be assumed to be 1 in the following), $\hat{\sigma}_j^+$ ($\hat{\sigma}_j^-$) is the raising (lowering) operator of the j -th qubit, μ_j denotes the on-site potential, the site-dependent coupling κ_j takes the form $\kappa_j \approx f((j - j_h + 1/2)d)/4d$ with d being the lattice constant. Here, the function $f(x)$ is related to spacetime metric, which is given in the Eddington-Finkelstein coordinates $\{t, x\}$ as $ds^2 = f(x)dt^2 - 2dtdx$. The spatial position x is discretized as $x_j = (j - j_h)d$. Since the horizon locates at $f(x_h) = 0$ with $f'(x_h) > 0$, the horizon in our analogues model is then defined at site $j = j_h$ where $f(x_h) = 0$, but the sign of κ_j is different on its two sides of the horizon resulting in a black hole spacetime structure. One side of horizon is considered

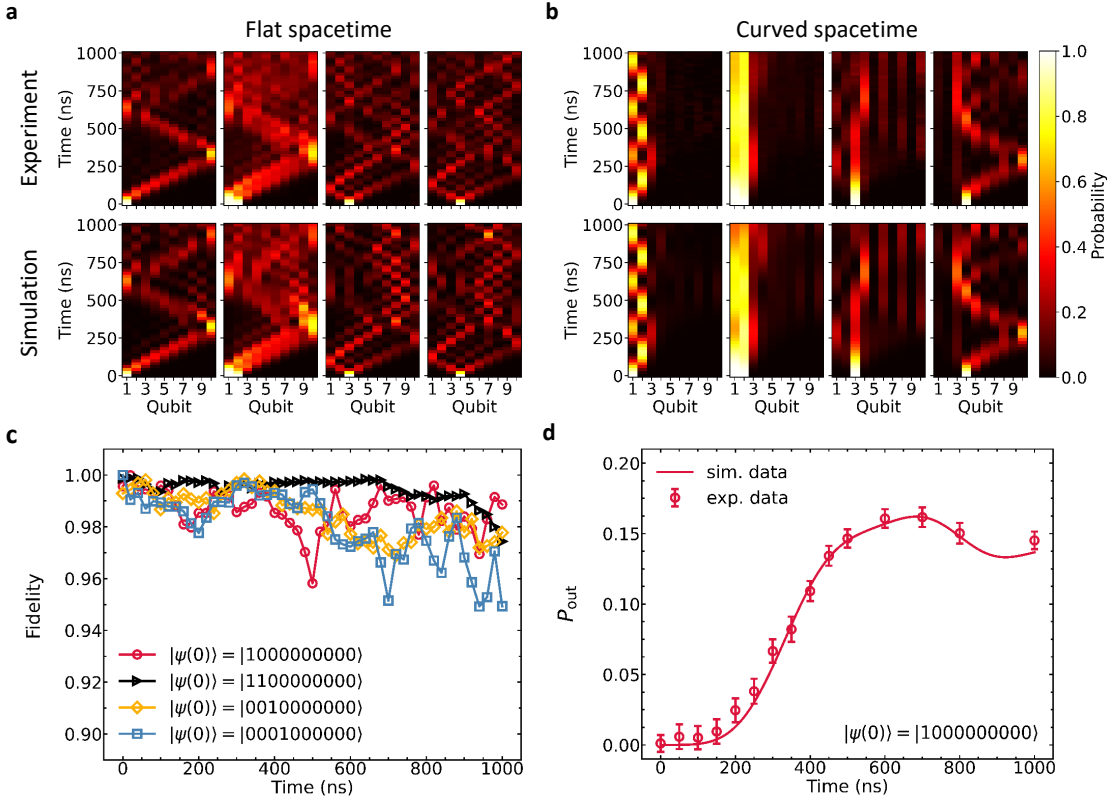


FIG. 2. **Quantum walks in a 1D array of 10 superconducting qubits.** **a**, Results of the quantum walks in a flat spacetime for four different initial states, i.e., $|\psi(0)\rangle = |1000000000\rangle$, $|1100000000\rangle$, $|0010000000\rangle$ and $|0001000000\rangle$ with $|0\rangle$ representing the ground state of a qubit and $|1\rangle$ the excited state. The case of black hole spacetime is presented in **b**. The heatmap denotes the probabilities of excited-state for Q_i in time. The horizontal axis is indexed as qubit number i , the vertical axis is the evolution time. Here we show both the numerical simulation and experiment data to compare the difference between the flat spacetime ($\kappa_j \approx 2.94$ MHz) and the curved spacetime ($\beta \approx 4.39$ MHz). **c**, The fidelity of quantum walks in the curved spacetime. **d**, The probability of finding a particle outside the horizon on qubits $\{Q_4Q_5Q_6Q_7Q_8Q_9Q_{10}\}$. Error bars are 1 SD calculated from all probability data of the $k = 1\text{-}50$ pulse sequences.

as the interior of the black hole, while the opposite side represents the exterior of the black hole.

We perform the experiment to simulate the black hole using a superconducting processor with a chain of 10 qubits $Q_1\text{-}Q_{10}$, which represents the Hamiltonian (2), additionally with 9 tunable couplers interspersed between every two nearest-neighbor qubits, see Fig. 1. The effective hopping coupling κ_j between qubits Q_j and Q_{j+1} , which derives from their direct capacitive coupling and the indirect virtual exchange coupling via the coupler in between, can be tuned arbitrarily via programming the frequency of the corresponding coupler C_j (see Supplementary and Ref. [19]). Additionally, we develop an efficient and automatic calibration for multi-qubit devices with tunable couplers to achieve accurate control of couplings (see Supplementary for details). To describe the curved spacetime experimentally, we change the frequencies of all the couplers by using the arbitrary waveform generator (AWG) to generate various flux-bias Z pulses applied to them, and design the effective coupling distri-

bution as

$$\kappa_j = \frac{\beta \tanh((j - j_h + 1/2)d)}{4d} \quad (3)$$

with $j_h = 3$, $d = 0.35$ a.u. and $\beta/(2\pi) \approx 4.39$ MHz. Here we choose $f(x) = \beta \tanh(x)$. As shown in Fig. 1b, the coupling κ_j goes monotonically from negative to positive from Q_3 's left to right side. In this way, the information of the static curved spacetime background is encoded into the site-dependent coupling distribution. Thus, the site Q_3 where the sign of the coupling reverses can be analogous to the event horizon of the black hole, the side of negative coupling ($Q_1\text{-}Q_2$) can be considered as the interior of the black hole, and $Q_4\text{-}Q_{10}$ are outside the horizon. For comparison, we also realize a uniform coupling distribution with $\kappa_j/(2\pi) \approx 2.94$ MHz to realize a flat spacetime.

In the experiment, we first prepare an initial state $|\psi(0)\rangle$ with quasi-particle excitations, i.e., exciting qubits or creating an entangled pair. The evolution of the initial state known as quantum walk will be governed by

Schrödinger equation $|\psi(t)\rangle = e^{-i\hat{H}t}|\psi(0)\rangle$ based on 1D programmable controlled Hamiltonian (2). The dynamics of the prepared states then simulates the behavior of quasi-particle in the studied (1+1)-dimensional spacetime with designed flat or curved structure.

Quantum walks in curved spacetime.—Figs. 2a and 2b show the propagation of quasi-particle in flat and curved spacetimes, respectively. Here we initialize the system by preparing four different single-particle or two-particle states, including $|\psi(0)\rangle = |1000000000\rangle$, $|1100000000\rangle$, $|0010000000\rangle$ and $|0001000000\rangle$ with $|0\rangle$ representing the ground state of a qubit and $|1\rangle$ the excited state. Once the initial state is prepared, we apply the rectangle Z pulses on each qubit to make the on-site potential μ_j of all qubits at a reference frequency $\omega_{\text{ref}}/(2\pi) \approx 5.1$ GHz. During the quench dynamics, the hopping couplings κ_j between qubits are fixed as Eq.(3) (curved spacetime) or a constant (flat spacetime) via biasing couplers. After time t , all qubits are biased back to idle points for readout. The occupation of quasi-particle density distribution $p_j(t) := \langle\psi(t)|\hat{\sigma}_j^+\hat{\sigma}_j^-|\psi(t)\rangle$ is measured by averaging 5000 repeated single-shot measurements, as shown in Figs. 2a and 2b for four initial states.

Fig. 2a shows that the propagation of quasi-particle in the flat spacetime is unimpeded, corresponding to the result of conventional quantum walk with diffusive expansion [25–28]. In contrast, the particle is mainly trapped in our on-chip black hole due to the analogue gravity around the horizon Q_3 , as shown in Fig. 2b with the initial state $|\psi(0)\rangle = |1000000000\rangle$ and $|\psi(0)\rangle = |1100000000\rangle$. Due to the infalling Eddington-Finkelstein coordinates we took, our model only simulates the outgoing modes of the particle (see Supplementary). Hence, the interior and exterior of black hole is equivalent so that the same phenomenon can be observed in that case where the particle is initially prepared in the exterior of black hole ($|\psi(0)\rangle = |0001000000\rangle$).

Here, we also present the result of the particle initialized at the horizon in Fig. 2b, i.e., $|\psi(0)\rangle = |0010000000\rangle$. In the continuous curved spacetime, the particle initialized at the horizon is bound to the horizon forever due to the zero couplings on both sides of the horizon. However, in the finite-size lattice, the coupling strengths on both sides of the horizon are not strictly zero even though they are very small (≈ 0.54 MHz). The particle seems to be localized at the horizon for a very short time, but it is doomed to escape from the constraints due to the finite-size effects.

To show the accuracy of the experimental results of quantum walk in the curved spacetime, we present the fidelity $F(t) = \sum_{j=1}^{10} \sqrt{p_j(t)q_j(t)}$ between the measured and theoretical probability distributions $p_j(t)$ and $q_j(t)$ in Fig. 2c. The high fidelity, greater than 97% within 400 ns experiment time, implies that our experimental results are consistent with the theoretical predictions as also demonstrated by the similarity between experimen-

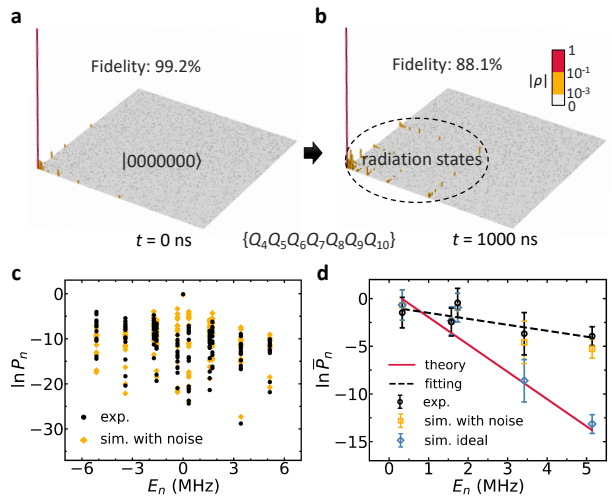


FIG. 3. **Observation of analogue Hawking radiation.** **a**, The 7-qubit density matrix at $t = 0$ ns. Initially, only Q_1 is prepared in $|1\rangle$ and all the qubits outside the horizon are almost in $|0\rangle$. **b**, The 7-qubit density matrix at $t = 1000$ ns after the quench dynamics. Due to the Hawking radiation, radiation states can be detected with small probabilities. The fidelity between ideal and experimental density matrix at $t = 0$ and 1000 ns are 99.2% and 88.1%, respectively. **c**, The logarithmic probability of finding a particle outside the horizon P_n vs. its energy E_n . **d**, The logarithm of average radiation probability vs. the energy of particle when $E_n > 0$. Error bars are 1 SD calculated from the tomography data at the same energy. The slope of the red line represents the reciprocal of Hawking temperature without noise, where the Hawking temperature here is given by $T_H/(2\pi) = \beta/(8\pi^2) \approx 0.35$ MHz or $\approx 1.7 \times 10^{-5}$ K in Kelvin temperature. The experimental results are in agreement with the simulated data for low energy, but diverge at high energy due to experiment noises.

tal data and numerical simulations. Note that in both cases of the flat and curved spacetimes the particle will be reflected when it arrives at the boundary Q_1 or Q_{10} .

Observation of Hawking radiation.—Black holes emit thermal radiation leading to evaporation, known as Hawking radiation. However, its observation is a challenge even for an analogue black hole due to the accuracy of the experiment.

For the initial state with a particle inside the horizon in our experiment, the evolution of the state shows the propagation of particle which results in nonzero density of state outside the horizon is equivalent to the Hawking radiation of the black hole. Defining the probability of finding a particle outside the horizon as $P_{\text{out}} = \sum_{j=4}^{10} p_j$, Fig. 2d shows a rising tendency of P_{out} in time. This result can be considered as an important signature of Hawking radiation for the analogue black hole [3, 4, 12, 29].

The theory of Hawking radiation points out that the probability of radiation satisfies a canonical blackbody

spectrum,

$$P_{\text{out}}(E) \propto e^{-\frac{E}{T_{\text{H}}}}, \quad (4)$$

where E denotes the energy of particle outside the horizon, $T_{\text{H}}/(2\pi) = g_{\text{h}}/(4\pi^2)$ is defined as the effective temperature of the Hawking radiation, and $g_{\text{h}} = \frac{1}{2}f'(x_{\text{h}}) = \beta/2$ represents the surface gravity of the black hole [18]. The derivation of Eq. (4) can be constructed by using the picture of quantum tunneling to obtain the tunneling rate of particle [30–32]. We use this picture in this work to understand the Hawking radiation. Such a picture is equivalent to a field theoretical viewpoint of “particle-antiparticle pairs” created around the horizon: the antiparticle (negative energy) falls into the black hole and annihilates with this particle inside the black hole, the particle outside the horizon is materialized and escapes into infinity (see Supplementary). Also, Eq. (4) can be viewed as the detailed balance relation between creation and annihilation of particle around the horizon in a thermal environment [33].

In Fig. 3a and 3b, we present the density matrix of 7 qubits Q_4 – Q_{10} by quantum state tomography (QST) at $t = 0$ and $t = 1000$ ns, such a final time is long enough so that the particle inside the black hole has finished its tunelling to the outside but the boundary effect is negligible to the results. Here, the initial state is $|\psi(0)\rangle = |1000000000\rangle$, i.e., a particle in the black hole has a certain position. When $t = 0$ ns, no radiation can be detected and all the qubits outside the horizon are almost in $|0\rangle$, see Fig. 3a. After a long time $t = 1000$ ns, one may have a small chance to probe the particle outside the horizon, see Fig. 3b. The corresponding probabilities of radiation can be extracted from the measured 7-qubit density matrix. Assuming that $|E_n\rangle$ is the n -th eigenenergy of total Hamiltonian and ρ_{out} is the density matrix outside obtained by QST, then the probability of finding a particle of energy E_n outside the horizon can be obtained as,

$$P_n = \langle E_n | \rho_{\text{out}} | E_n \rangle. \quad (5)$$

Although there are $2^{10} = 1024$ eigenstates for 10-qubit Hamiltonian Eq. (2) and the same number of P_n , the radiation states involve only 10 single-particle excited eigenstates due to the particle number conservation. As a consequence, only those P_n that are corresponding to single-particle excited eigenstates have non-zero values, as shown in Fig. 3c. Therefore, we take the average of P_n with the same positive energy E_n as \bar{P}_n to describe the average probability of finding a particle outside with $E_n > 0$. It can be expected that the relation between \bar{P}_n and E_n will agree with the theoretical prediction in Eq. (4). In Fig. 3d, the simulated results show that the logarithm of the average radiation probability is approximately linear in energy with Hawking temperature 1.7×10^{-5} K. The fitted Hawking temperature of

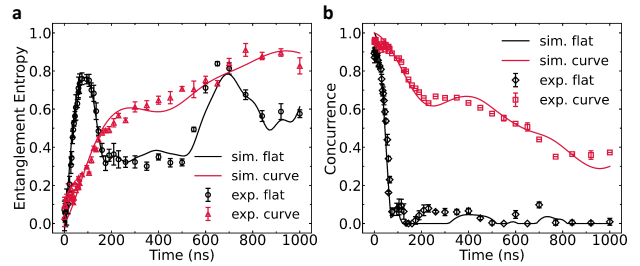


FIG. 4. **Dynamics of entanglement in the analogue black hole.** a, The entanglement entropy vs. evolution time in different spacetimes. The entanglement entropy gradually increases with time in the curved spacetime, corresponding to the early time of Page curve. b, The concurrence (Entanglement between the pair in black hole) vs. evolution time in different spacetimes. Error bars are 1 SD calculated from all tomography data of the $k = 1$ –10 pulse sequences. The rapid decline of concurrence in the flat spacetime is observed, while the concurrence in the curved spacetime is protected due to the analogue gravity. The solid lines are the results of numerical simulation. Here we set the coupling for the flat spacetime to be a constant ($\kappa \approx 2.94$ MHz) and $\beta/(2\pi) \approx 4.39$ MHz for the curved spacetime.

experimental data is around $\sim 7.7 \times 10^{-5}$ K, showing validity with the same order of magnitude. The deviation between experimental data and ideal simulation data is mainly caused by the evolution of the imperfect initial state. The fidelity between the imperfect initial state in experiment and ideal initial state is 99.2%, which may derive from the experimental noises including XY crosstalk, thermal excitation, leakage, etc. We substitute such a experimental state for the ideal initial state in the numerical simulation of Hawking radiation, then the results of numerical simulation agree with experimental results better.

Note that the simulated black hole here is one-dimensional in space. It may be difficult to define mass. If we consider a black hole in four-dimensional spacetime with the same Hawking temperature T_{H} , its mass can be calculated by $M/M_{\text{s}} = 6.4 \times 10^{-8} \text{ K}/T_{\text{H}}$ [1], where $M_{\text{s}} \approx 2 \times 10^{30}$ kg is the solar mass. For the simulated black hole here, its mass is about one thousandth of the solar mass.

Dynamics of entanglement in the analogue black hole.—Hawking predicted that the entanglement entropy increases when a black hole forms and evaporates due to the Hawking radiation. Each Hawking particle is entangled with a partner particle in the black hole. Such kind of quantum feature plays a crucial role in studying black holes and quantum information [34].

To investigate the dynamical entanglement and non-local correlation both in flat spacetime and curved space-time, we perform the time-dependent QST measurement on reduced quantum states of two qubits (Q_1 & Q_2) in the black hole. We focus on two quantities, entanglement en-

tropy and concurrence. Both of them can be computed by using the two-qubit density matrix $\rho_{in}(t)$ with time t obtained by the results of QST. Here, the entanglement entropy is given by $S(t) = -\text{Tr}[\rho(t) \ln \rho(t)]$ quantifying the entanglement between the interior of black hole and the exterior [35]. The concurrence represents the entanglement just between the two qubits in the black hole, which is calculated as $E(\rho) = \max\{0, \lambda_1 - \lambda_2 - \lambda_3 - \lambda_4\}$ with λ_i being the square roots of the eigenvalues of matrix $\rho\tilde{\rho}$ in decreasing order, where $\tilde{\rho} = (\hat{\sigma}_y \otimes \hat{\sigma}_y)\rho^*(\hat{\sigma}_y \otimes \hat{\sigma}_y)$ is the spin-flipped state of ρ with σ_y being Pauli matrix [36].

As shown in Fig. 1c, we first prepare an entangled pair in our on-chip black hole by implementing a $\pi/2$ pulse (along the Y -axis of the Bloch sphere) on control qubit Q_1 and a subsequent controlled-NOT (CNOT) gate on the pair. The CNOT gate includes a $-\pi/2$ pulse on target qubit Q_2 , an adiabatic controlled-phase (CZ) gate and a $Y/2$ gate on Q_2 in sequence. We realize the CZ gate with the tunable coupler by using the recent developed approach of adiabatic CZ gate [20–22]. The mean fidelity of prepared Bell state $(|00\rangle + |11\rangle)/\sqrt{2}$ is 99.15%.

Figure 4 shows the dynamics of such an initial entangled state in both the flat and curved spacetime. Here we choose a relatively small β to reduce the propagation speed of particle that escapes from the black hole and the finite size effect thus will be reduced during the quench dynamics. In Fig. 4a, the entanglement entropy in the case of curved spacetime progressively increases due to the Hawking radiation, while in the flat spacetime it has two wavefronts resulting from the quantum interference and reflection respectively [27]. On the other hand, the concurrence decreases with time in both cases, reflecting the process of entanglement being lost into the environment. However, the entanglement between the pair in the black hole is protected by the analogue gravity so that it can slow the decrease of the concurrence, see Fig. 4b.

Summary and outlook.—In summary, we have experimentally simulated a curved spacetime of black hole and observed Hawking radiation in a superconducting processor with tunable couplers. Our results would stimulate further interests to explore related problems such as different designed curved spacetime and time-evolving black holes [34, 37–39]. A more advanced processor with more qubits in 1D array may reduce the finite-size effects, and provides more accurate data in simulating black holes. A 2D quantum processor may facilitate the simulation of other properties of black holes such as gravitational lensing and slingshot, the relationship between entropy and black hole horizon area.

This work was supported by the Synergetic Extreme Condition User Facility (SECUF). Devices were made at the Nanofabrication Facilities at Institute of Physics in Beijing. **Funding:** Supported by National Natural Science Foundation of China (Grant Nos. T2121001, 11774406, 11934018, 12005155, 11904393 and 92065114),

the State Key Development Program for Basic Research of China (Grant No. 2017YFA0304300), the Key-Area Research and Development Program of Guangdong Province, China (Grant No. 2020B0303030001), the Strategic Priority Research Program of Chinese Academy of Sciences (Grant No. XDB28000000), Scientific Instrument Developing Project of Chinese Academy of Sciences (Grant No. YJKYYQ20200041), and Beijing Natural Science Foundation (Grant No. Z200009).

Author contributions: Y.-H.S. performed the experiment with the assistance of K.X.; R.-G.C. and H.F. conceived the idea; R.-Q.Y. and R.-G.C. provided theoretical support; K.X., Y.-H.S., R.-Q.Y., Z.-Y.G. and Y.-Y.W. performed the numerical simulation; Z.X. fabricated the device with the help of D.Z. and X.S.; Y.-H.S., H.L. and K.H. helped the experimental setup supervised by K.X. with the assistance of Y.T.; H.F. supervised the whole project; Y.-H.S., R.-Q.Y., Y.-Y.W., Z.-Y.G., R.-G.C. and H.F. cowrote the manuscript, and all authors contributed to the discussions of the results and development of the manuscript. **Competing interests:** Authors declare no competing interests. **Data availability:** The data that support the plots within this paper and other findings of this study are available from the author upon reasonable request.

* These authors contributed equally to this work.

† dzheng@iphy.ac.cn

‡ kaixu@iphy.ac.cn

§ cairg@itp.ac.cn

¶ hfan@iphy.ac.cn

- [1] S. W. Hawking, Black hole explosions?, *Nature* **248**, 30 (1974).
- [2] W. G. Unruh, Experimental Black-Hole Evaporation?, *Phys. Rev. Lett.* **46**, 1351 (1981).
- [3] W. G. Unruh, Sonic analogue of black holes and the effects of high frequencies on black hole evaporation, *Phys. Rev. D* **51**, 2827 (1995).
- [4] S. Weinfurtner, E. W. Tedford, M. C. J. Penrice, W. G. Unruh, and G. A. Lawrence, Measurement of Stimulated Hawking Emission in an Analogue System, *Phys. Rev. Lett.* **106**, 021302 (2011).
- [5] F. Michel and R. Parentani, Probing the thermal character of analogue Hawking radiation for shallow water waves?, *Phys. Rev. D* **90**, 044033 (2014).
- [6] L.-P. Euvé, F. Michel, R. Parentani, and G. Rousseaux, Wave blocking and partial transmission in subcritical flows over an obstacle, *Phys. Rev. D* **91**, 024020 (2015).
- [7] A. Coutant and S. Weinfurtner, The imprint of the analogue Hawking effect in subcritical flows, *Phys. Rev. D* **94**, 064026 (2016).
- [8] O. Lahav, A. Itah, A. Blumkin, C. Gordon, S. Rinott, A. Zayats, and J. Steinhauer, Realization of a Sonic Black Hole Analog in a Bose-Einstein Condensate, *Phys. Rev. Lett.* **105**, 240401 (2010).
- [9] J. Steinhauer, Observation of quantum Hawking radiation and its entanglement in an analogue black hole, *Na-*

ture Physics **12**, 959 (2016).

[10] J. R. Muñoz de Nova, K. Golubkov, V. I. Kolobov, and J. Steinhauer, Observation of thermal Hawking radiation and its temperature in an analogue black hole, *Nature* **569**, 688 (2019).

[11] T. G. Philbin, C. Kuklewicz, S. Robertson, S. Hill, F. Konig, and U. Leonhardt, Fiber-Optical Analog of the Event Horizon, *Science* **319**, 1367 (2008).

[12] J. Drori, Y. Rosenberg, D. Bermudez, Y. Silberberg, and U. Leonhardt, Observation of Stimulated Hawking Radiation in an Optical Analogue, *Phys. Rev. Lett.* **122**, 010404 (2019).

[13] C. Sheng, H. Liu, Y. Wang, S. N. Zhu, and D. A. Genov, Trapping light by mimicking gravitational lensing, *Nature Photonics* **7**, 902 (2013).

[14] F. Arute, K. Arya, R. Babbush, D. Bacon, J. C. Bardin, R. Barends, R. Biswas, S. Boixo, F. G. S. L. Brandao, D. A. Buell, B. Burkett, Y. Chen, Z. Chen, B. Chiaro, R. Collins, W. Courtney, A. Dunsworth, E. Farhi, B. Foxen, A. Fowler, C. Gidney, M. Giustina, R. Graff, K. Guerin, S. Habegger, M. P. Harrigan, M. J. Hartmann, A. Ho, M. Hoffmann, T. Huang, T. S. Humble, S. V. Isakov, E. Jeffrey, Z. Jiang, D. Kafri, K. Kechedzhi, J. Kelly, P. V. Klimov, S. Knysh, A. Korotkov, F. Kostritsa, D. Landhuis, M. Lindmark, E. Lucero, D. Lyakh, S. Mandrà, J. R. McClean, M. McEwen, A. Megrant, X. Mi, K. Michelsen, M. Mohseni, J. Mutus, O. Naaman, M. Neeley, C. Neill, M. Y. Niu, E. Ostby, A. Petukhov, J. C. Platt, C. Quintana, E. G. Rieffel, P. Roushan, N. C. Rubin, D. Sank, K. J. Satzinger, V. Smelyanskiy, K. J. Sung, M. D. Trevithick, A. Vainsencher, B. Villalonga, T. White, Z. J. Yao, P. Yeh, A. Zalcman, H. Neven, and J. M. Martinis, Quantum supremacy using a programmable superconducting processor, *Nature* **574**, 505 (2019).

[15] I. M. Georgescu, S. Ashhab, and F. Nori, Quantum simulation, *Rev. Mod. Phys.* **86**, 153 (2014).

[16] X. Gu, A. F. Kockum, A. Miranowicz, Y. xi Liu, and F. Nori, Microwave photonics with superconducting quantum circuits, *Physics Reports* **718-719**, 1 (2017).

[17] Y. Wu, W.-S. Bao, S. Cao, F. Chen, M.-C. Chen, X. Chen, T.-H. Chung, H. Deng, Y. Du, D. Fan, M. Gong, C. Guo, C. Guo, S. Guo, L. Han, L. Hong, H.-L. Huang, Y.-H. Huo, L. Li, N. Li, S. Li, Y. Li, F. Liang, C. Lin, J. Lin, H. Qian, D. Qiao, H. Rong, H. Su, L. Sun, L. Wang, S. Wang, D. Wu, Y. Xu, K. Yan, W. Yang, Y. Yang, Y. Ye, J. Yin, C. Ying, J. Yu, C. Zha, C. Zhang, H. Zhang, K. Zhang, Y. Zhang, H. Zhao, Y. Zhao, L. Zhou, Q. Zhu, C.-Y. Lu, C.-Z. Peng, X. Zhu, and J.-W. Pan, Strong Quantum Computational Advantage Using a Superconducting Quantum Processor, *Physical Review Letters* **127**, 180501 (2021).

[18] R.-Q. Yang, H. Liu, S. Zhu, L. Luo, and R.-G. Cai, Simulating quantum field theory in curved spacetime with quantum many-body systems, *Phys. Rev. Research* **2**, 023107 (2020).

[19] F. Yan, P. Krantz, Y. Sung, M. Kjaergaard, D. L. Campbell, T. P. Orlando, S. Gustavsson, and W. D. Oliver, Tunable Coupling Scheme for Implementing High-Fidelity Two-Qubit Gates, *Phys. Rev. Applied* **10**, 054062 (2018).

[20] Y. Sung, L. Ding, J. Braumüller, A. Vepsäläinen, B. Kanman, M. Kjaergaard, A. Greene, G. O. Samach, C. McNally, D. Kim, A. Melville, B. M. Niedzielski, M. E. Schwartz, J. L. Yoder, T. P. Orlando, S. Gustavsson, and W. D. Oliver, Realization of High-Fidelity CZ and ZZ-Free iSWAP Gates with a Tunable Coupler, *Phys. Rev. X* **11**, 021058 (2021).

[21] Y. Xu, J. Chu, J. Yuan, J. Qiu, Y. Zhou, L. Zhang, X. Tan, Y. Yu, S. Liu, J. Li, F. Yan, and D. Yu, High-Fidelity, High-Scalability Two-Qubit Gate Scheme for Superconducting Qubits, *Phys. Rev. Lett.* **125**, 240503 (2020).

[22] M. C. Collodo, J. Herrmann, N. Lacroix, C. K. Andersen, A. Remm, S. Lazar, J.-C. Besse, T. Walter, A. Wallraff, and C. Eichler, Implementation of Conditional Phase Gates Based on Tunable ZZ Interactions, *Phys. Rev. Lett.* **125**, 240502 (2020).

[23] R. B. Mann, S. M. Morsink, A. E. Sikkema, and T. G. Steele, Semiclassical gravity in 1+1 dimensions, *Phys. Rev. D* **43**, 3948 (1991).

[24] J. S. Pedernales, M. Beau, S. M. Pittman, I. L. Egusquiza, L. Lamata, E. Solano, and A. del Campo, Dirac Equation in (1+1)-Dimensional Curved Spacetime and the Multiphoton Quantum Rabi Model, *Phys. Rev. Lett.* **120**, 160403 (2018).

[25] A. M. Childs, Universal Computation by Quantum Walk, *Physical Review Letters* **102**, 180501 (2009).

[26] M. Karski, L. Förster, J.-M. Choi, A. Steffen, W. Alt, D. Meschede, and A. Widera, Quantum Walk in Position Space with Single Optically Trapped Atoms, *Science* **325**, 174 (2009).

[27] Z. Yan, Y.-R. Zhang, M. Gong, Y. Wu, Y. Zheng, S. Li, C. Wang, F. Liang, J. Lin, Y. Xu, C. Guo, L. Sun, C.-Z. Peng, K. Xia, H. Deng, H. Rong, J. Q. You, F. Nori, H. Fan, X. Zhu, and J.-W. Pan, Strongly correlated quantum walks with a 12-qubit superconducting processor, *Science* **364**, 753 (2019).

[28] M. Gong, S. Wang, C. Zha, M.-C. Chen, H.-L. Huang, Y. Wu, Q. Zhu, Y. Zhao, S. Li, S. Guo, H. Qian, Y. Ye, F. Chen, C. Ying, J. Yu, D. Fan, D. Wu, H. Su, H. Deng, H. Rong, K. Zhang, S. Cao, J. Lin, Y. Xu, L. Sun, C. Guo, N. Li, F. Liang, V. M. Bastidas, K. Nemoto, W. J. Munro, Y.-H. Huo, C.-Y. Lu, C.-Z. Peng, X. Zhu, and J.-W. Pan, Quantum walks on a programmable two-dimensional 62-qubit superconducting processor, *Science* **372**, 948 (2021).

[29] R. Brout, S. Massar, R. Parentani, and P. Spindel, Hawking radiation without trans-Planckian frequencies, *Phys. Rev. D* **52**, 4559 (1995).

[30] T. Damour and R. Ruffini, Black-hole evaporation in the Klein-Sauter-Heisenberg-Euler formalism, *Phys. Rev. D* **14**, 332 (1976).

[31] M. K. Parikh and F. Wilczek, Hawking Radiation As Tunneling, *Phys. Rev. Lett.* **85**, 5042 (2000).

[32] M. Arzano, A. J. M. Medved, and E. C. Vagenas, Hawking radiation as tunneling through the quantum horizon, *Journal of High Energy Physics* **9**, 037 (2005).

[33] P. D. Nation, J. R. Johansson, M. P. Blencowe, and F. Nori, Colloquium: Stimulating uncertainty: Amplifying the quantum vacuum with superconducting circuits, *Rev. Mod. Phys.* **84**, 1 (2012).

[34] J. Maldacena, Black holes and quantum information, *Nature Reviews Physics* **2**, 123 (2020).

[35] V. Vedral, M. B. Plenio, M. A. Rippin, and P. L. Knight, Quantifying Entanglement, *Phys. Rev. Lett.* **78**, 2275 (1997).

[36] W. K. Wootters, Entanglement of Formation of an Ar-

bitrary State of Two Qubits, *Phys. Rev. Lett.* **80**, 2245 (1998).

[37] J. Polchinski, The Black Hole Information Problem, in *New Frontiers in Fields and Strings* (WORLD SCIENTIFIC, 2017) pp. 353–397.

[38] A. Almheiri, T. Hartman, J. Maldacena, E. Shaghoulian, and A. Tajdini, Replica wormholes and the entropy of Hawking radiation, *Journal of High Energy Physics* **5**, 13 (2020).

[39] D. N. Page, Information in black hole radiation, *Phys. Rev. Lett.* **71**, 3743 (1993).

[40] E. Lieb, T. Schultz, and D. Mattis, Two soluble models of an antiferromagnetic chain, *Annals of Physics* **16**, 407 (1961).

[41] R. B. Mann, S. M. Morsink, A. E. Sikkema, and T. G. Steele, Semiclassical gravity in 1+1 dimensions, *Phys. Rev. D* **43**, 3948 (1991).

[42] J. Koch, T. M. Yu, J. Gambetta, A. A. Houck, D. I. Schuster, J. Majer, A. Blais, M. H. Devoret, S. M. Girvin, and R. J. Schoelkopf, Charge-insensitive qubit design derived from the Cooper pair box, *Physical Review A* **76**, 042319 (2007).

[43] P. Krantz, M. Kjaergaard, F. Yan, T. P. Orlando, S. Gustavsson, and W. D. Oliver, A quantum engineer’s guide to superconducting qubits, *Applied Physics Reviews* **6**, 021318 (2019).

[44] S. Kwon, A. Tomonaga, G. Lakshmi Bhai, S. J. Devitt, and J.-S. Tsai, Gate-based superconducting quantum computing, *Journal of Applied Physics* **129**, 041102 (2021).

[45] M. A. Rol, L. Ciorciaro, F. K. Malinowski, B. M. Tarasinski, R. E. Sagastizabal, C. C. Bultink, Y. Salathe, N. Haandbaek, J. Sedivy, and L. DiCarlo, Time-domain characterization and correction of on-chip distortion of control pulses in a quantum processor, *Applied Physics Letters* **116**, 054001 (2020).

[46] X. Li, T. Cai, H. Yan, Z. Wang, X. Pan, Y. Ma, W. Cai, J. Han, Z. Hua, X. Han, Y. Wu, H. Zhang, H. Wang, Y. Song, L. Duan, and L. Sun, Tunable Coupler for Realizing a Controlled-Phase Gate with Dynamically Decoupled Regime in a Superconducting Circuit, *Physical Review Applied* **14**, 024070 (2020).

[47] H. Xu, W. Liu, Z. Li, J. Han, J. Zhang, K. Linghu, Y. Li, M. Chen, Z. Yang, J. Wang, T. Ma, G. Xue, Y. Jin, and H. Yu, Realization of adiabatic and diabatic CZ gates in superconducting qubits coupled with a tunable coupler, *Chinese Physics B* **30**, 044212 (2021).

Supplementary Material: On-chip black hole: Hawking radiation and curved spacetime in a superconducting circuit with tunable couplers

INTRODUCTION ON EDDINGTON-FINKELSTEIN COORDINATES

In this paper, the spacetime geometry is present by advanced Eddington-Finkelstein coordinates (AEFC) $\{t, x\}$. Though the coordinate “ t ” plays the role of “time” in this system, there are a few of differences compared with the usually time coordinate. In this appendix, we will give a basic introduction.

One simple way to obtain an intuition of advanced Eddington-Finkelstein coordinates $\{v, x\}$ is to consider the wave propagating in flat spacetime. Let us consider a Minkowski spacetime. The usual Minkowski coordinates (MC) is $\{t_m, x\}$, of which the metric reads

$$ds^2 = dt_m^2 - dx^2 \quad (S1)$$

The massless scalar field then will satisfies

$$\partial_{t_m}^2 \phi - \partial_x^2 \phi = 0 \quad (S2)$$

The solution of this equation in general is given by following “traveling wave solution”,

$$\phi(t_m, x) = \phi_1(t_m + x) + \phi_2(t_m - x), \quad (S3)$$

where $\phi_1(t_m + x)$ stands for the advanced solution and $\phi_2(t_m - x)$ stands for the outgoing solution.

To convert the advanced Eddington-Finkelstein coordinates $\{t, x\}$, we consider a coordinates transformation

$$t = t_m + x, \quad (S4)$$

and so the metric then reads

$$ds^2 = dt^2 - 2dtdx. \quad (S5)$$

It needs to note that, though $dt_m \neq dt$, we still have

$$\partial_{t_m} h|_{MC} = \partial_t h|_{AEFC}, \quad (S6)$$

for arbitrary function h , i.e. the time derivatives are the same as that in the usual Minkowski coordinates and advanced Eddington-Finkelstein coordinates. Thus, the growth rate of a quantity in usual Minkowski coordinates can also be computed according to the time derivative of advanced Eddington-Finkelstein coordinates. On the contrary, if one wants to compute the spatial derivative, then the two coordinate systems will have different results

$$\partial_x h|_{MC} \neq \partial_x h|_{AEFC} \quad (S7)$$

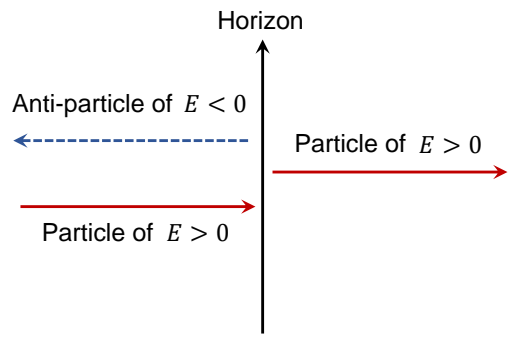


FIG. S1. The anti-particle flow of negative energy infalling toward the interior of black hole can always be interpreted as a particle flow of positive energy outgoing from the interior.

in general since the derivative in left-side fixes t_m but the derivative of right-side fixes $t = t_m + x$.

The propagators of wave are also very different in these two coordinate systems. From Eq. (S3), one sees that the “traveling wave solution” in advanced Eddington-Finkelstein coordinates reads

$$\phi(t, x) = \phi_1(t) + \phi_2(t - 2x), \quad (S8)$$

This can also be obtained from the wave equation $2\partial_t \partial_x \phi + 2\partial_x^2 \phi = 0$. It is a little surprising that the advanced wave ϕ_1 has no propagator! In fact *the infalling mode now becomes a boundary condition rather than a propagator*. If we impose a boundary condition

$$\phi(t, \pm\infty) = 0, \quad (S9)$$

then we have $\phi_1(t) = 0$ and so there is only outgoing mode. Thus, the advanced Eddington-Finkelstein coordinates with boundary condition (S9) can only represent the propagator of outgoing modes. In other words, the advanced Eddington-Finkelstein coordinates play the role of selector to choose only outgoing modes.

Though we assume that the spacetime is flat and the matter is scalar field in above discussion, the basic physical picture will still be true if we consider a curved 2-dimensional spacetime and Dirac field. From the Fig. 2 in our main-context, one can see that our model only simulates the outgoing modes, just as we expected in above discussion. In general, the wave in gravitational fields contains both advanced modes and outgoing modes. The Hawking radiation is an energy flux towards infinity, i.e. carried by outgoing modes. This is one reason why this paper uses advanced Eddington-Finkelstein coordinates to study the Hawking radiation.

MORE EXPLANATION ON THE “TUNNELING PICTURE” OF HAWKING RADIATION

In this paper, we use the picture of “quantum tunneling” to understand the Hawking radiation [30–32].

Though this is also a wide spread picture to understand Hawking radiation in the community of black hole physics, it may not be familiar to the other readers. Here we make a brief introduction on this picture.

A first glance, the tunneling picture is very different from picture of “pair creation” outside horizon. However, they are equivalent in physics. Based on the picture of “pair creation” in Hawking radiation, “particle-antiparticle pairs” can be created around the horizon. The antiparticle (negative energy) falls into the black hole and annihilates with positive energy particle inside the black hole, the particle outside the horizon is materialized and escapes into infinity. Note that the pair creation/annihilation is a virtual process, and the really materialized result is that the original particle inside the black hole disappears but an identical particle appears outside the horizon. The anti-particle of negative energy infalling the interior of black hole can always be interpreted as a particle of positive energy outgoing from the interior, see schematic diagram Fig. S1. This leads to an equivalent picture to understand Hawking radiation via quantum tunneling: the particle inside the horizon escapes to outside by quantum tunneling. Thus, the “tunneling picture” and “pair creation picture” are just two different pictures to understand the same physical phenomenon. Note that this “tunneling picture” does not violate causality since the spectrum is thermal and no information is carried.

Let us explain in detail about how to use this tunneling picture to obtain the spectrum of radiation and corresponding temperature. For the spacetime with a black hole, the metric in the Schwarzschild coordinates $\{t_s, x\}$ is given by $ds^2 = f(x)dt_s^2 - f^{-1}(x)dx^2$. We consider an outgoing mode with positive energy (corresponding to the observers of infinity) of a massless scalar or Dirac field, which can be written as

$$\Phi(t_s, x) \propto \exp \left[-i\omega \left(t_s - \int \frac{dx}{f(x)} \right) \right]. \quad (\text{S10})$$

By using the Eddington-Finkelstein coordinates we have

$$\Phi(t, x) \propto \exp \left[-i\omega \left(t - 2 \int \frac{dx}{f(x)} \right) \right]. \quad (\text{S11})$$

Since $f(x)$ has a root at $f(x_h)$, we separate integration

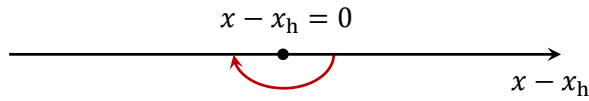


FIG. S2. The wavefunction are connected in the complex plane $\ln|x_h - x| \rightarrow \ln|x_h - x| - i\pi$ when x runs from outside horizon into inside horizon, which yields $|x_h - x|^{i\omega/g_h} \rightarrow |x_h - x|^{i\omega/g_h} e^{\pi\omega/g_h}$.

into two parts,

$$\int \frac{dx}{f(x)} = F(x) + \int \frac{dx}{2g_h(x - x_h)} = F(x) + \frac{1}{2g_h} \ln|x - x_h|, \quad (\text{S12})$$

where

$$F(x) = \int \left[\frac{1}{f(x)} - \frac{1}{2g_h(x - x_h)} \right] dx \quad (\text{S13})$$

is regular at $x = x_h$. Here $g_h = f'(x_h)/2$ is the surface gravity. Thus, the outgoing positive mode then reads

$$\Phi(t, x) \propto e^{-i\omega[t-2F(x)]} |x - x_h|^{i\omega/g_h}. \quad (\text{S14})$$

This outgoing mode has an infinite number of oscillations as $x \rightarrow x_h$ and therefore cannot be straightforwardly extended to the inner region from the region outside horizon. As argued in Ref. [30], we can use analytic continuation to connected two branches in complex plane: the wave function Φ describing a particle state (positive frequencies) can be analytically continued to complex plane (see Fig. S2). Then we obtain

$$\Phi(t, x) = \begin{cases} e^{-i\omega[t-2F(x)]} |x - x_h|^{i\omega/g_h}, & x > x_h \\ e^{-i\omega[t-2F(x)]} |x_h - x|^{i\omega/g_h} e^{\pi\omega/g_h}, & x < x_h. \end{cases} \quad (\text{S15})$$

This gives us the tunneling rate

$$P = e^{-2\pi\omega/g_h}, \quad (\text{S16})$$

which is identical to the detailed balance relation for transition rates in a thermal environment [33]. Note that the tunneling rate (S16) stands for the rate of a single particle. It is possible that the tunneling of multiple particles happens simultaneously. For bosons we have

$$\begin{array}{cccccc} \text{particle number:} & 0 & 1 & 2 & 3 & \dots \\ \text{probability:} & 1 & P & P^2 & P^3 & \dots \end{array} \quad (\text{S17})$$

Thus the occupation number of energy ω reads

$$n(\omega) = \frac{\sum_{k=0}^{\infty} k P^k}{\sum_{k=0}^{\infty} P^k} = \frac{1}{e^{2\pi\omega/g_h} - 1}. \quad (\text{S18})$$

This gives us the expected distribution of bosons and the temperature reads $T = g_h/(2\pi)$ as predicted by Hawking. For fermions, if there is no other internal degree of freedom, the Pauli exclusion principle implies that there is at most one particle of same energy. Thus, Eq. (S17) is replaced by

$$\begin{array}{cccccc} \text{particle number } n : & 0 & 1 & & & \\ \text{probability:} & 1 & P & & & \end{array} \quad (\text{S19})$$

Thus the occupation number of energy ω reads

$$n(\omega) = \frac{\sum_{k=0}^1 k P^k}{\sum_{k=0}^1 P^k} = \frac{1}{e^{2\pi\omega/g_h} + 1}. \quad (\text{S20})$$

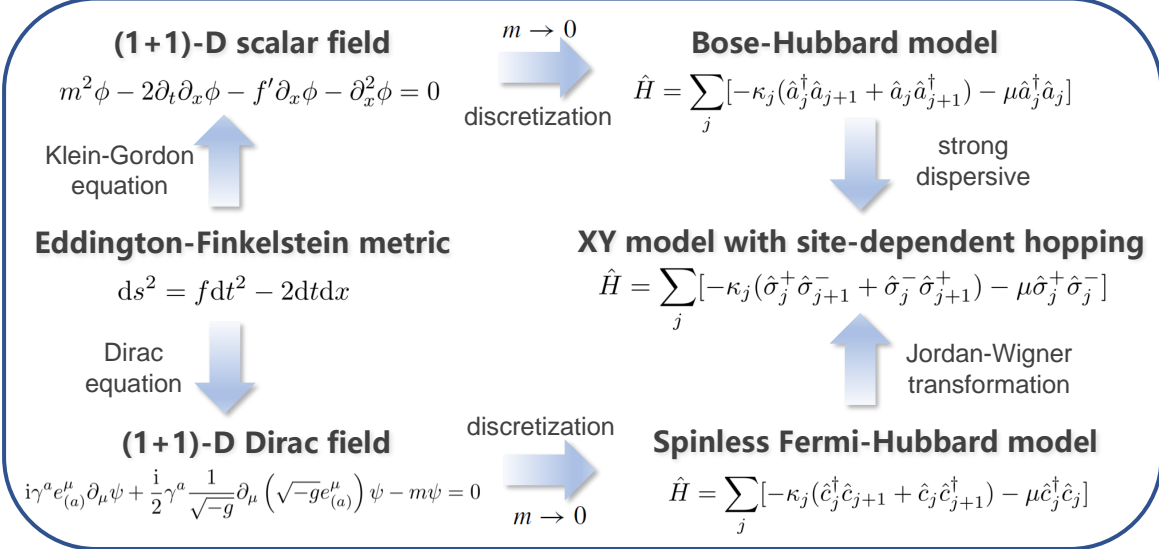


FIG. S3. The theoretical framework of simulating quantum field theory in (1+1)-D curved spacetime with quantum many-body systems. The “time” t in the infalling Eddington-Finkelstein metric is given by $t = t_s + \int f^{-1} dx$ where $\{t_s, x\}$ are the Schwarzschild coordinates. In (1+1)-D configurations, the massless scalar field ϕ and the massless Dirac field ψ can be discretized into the Bose-Hubbard model and the spinless Fermi-Hubbard model respectively, where the static curved spacetime background is encoded into the site-dependent hopping coupling distribution κ_j satisfying Eq. (S41). Here the on-site potential μ is an arbitrary constant. Note that both of the Bose-Hubbard model and the spinless Fermi-Hubbard model can be transformed into the XY model, which implies their equivalence in (1+1)-D spacetime. This schematic diagram is a brief summary of the theory in Ref. [18].

This gives us the expected distribution of fermions and the temperature still reads $T = g_h/(2\pi)$.

In addition, the composite system of the interior of black hole and the exterior is isolated. The interior and the exterior exchange energy and particles via the horizon. Hence, the occupations Eq. (S18) and (S20) can be viewed as the statistical averages of grand canonical distributions concerning bosons and fermions, respectively.

MODEL AND HAMILTONIAN

Our experiment is performed on a superconducting quantum processor which consists of 10 transmon qubits ($Q_1 \sim Q_{10}$) and 9 transmon-type couplers ($C_1 \sim C_9$). Each qubit and coupler are frequency-tunable, but only qubits have the XY control line and the readout resonator. The total Hamiltonian of this all-transmon system can be expressed as

$$\hat{H} = \hat{H}_Q + \hat{H}_C + \hat{H}_{Q-Q} + \hat{H}_{Q-C} + \hat{H}_{C-C}, \quad (S21)$$

$$\hat{H}_Q/\hbar = \sum_{j=1}^{10} \omega_{q_j} \hat{b}_{q_j}^\dagger \hat{b}_{q_j} + \frac{\alpha_{q_j}}{2} \hat{b}_{q_j}^\dagger \hat{b}_{q_j}^\dagger \hat{b}_{q_j} \hat{b}_{q_j}, \quad (S22)$$

$$\hat{H}_C/\hbar = \sum_{j=1}^9 \omega_{c_j} \hat{b}_{c_j}^\dagger \hat{b}_{c_j} + \frac{\alpha_{c_j}}{2} \hat{b}_{c_j}^\dagger \hat{b}_{c_j}^\dagger \hat{b}_{c_j} \hat{b}_{c_j}, \quad (S23)$$

$$\hat{H}_{Q-Q}/\hbar = \sum_{j=1}^9 g_{q_j, q_{j+1}} (\hat{b}_{q_j}^\dagger \hat{b}_{q_{j+1}} + \hat{b}_{q_j} \hat{b}_{q_{j+1}}^\dagger), \quad (S24)$$

$$\hat{H}_{C-C}/\hbar = \sum_{j=1}^9 g_{c_j, c_{j+1}} (\hat{b}_{c_j}^\dagger \hat{b}_{c_{j+1}} + \hat{b}_{c_j} \hat{b}_{c_{j+1}}^\dagger), \quad (S25)$$

$$\begin{aligned} \hat{H}_{Q-C}/\hbar = & \sum_{j=1}^9 g_{q_j, c_j} (\hat{b}_{q_j}^\dagger \hat{b}_{c_j} + \hat{b}_{q_j} \hat{b}_{c_j}^\dagger) \\ & + g_{q_{j+1}, c_j} (\hat{b}_{q_{j+1}}^\dagger \hat{b}_{c_j} + \hat{b}_{q_{j+1}} \hat{b}_{c_j}^\dagger), \end{aligned} \quad (S26)$$

where \hbar is the reduced Planck constant (for convenience \hbar will be assumed to be 1 in the following), \hat{b}_{q_j} (\hat{b}_{c_j}) and $\hat{b}_{q_j}^\dagger$ ($\hat{b}_{c_j}^\dagger$) denote the annihilation and creation operators of the j -th qubit (coupler), respectively. The corresponding frequencies and anharmonicities are ω_{q_j} (ω_{c_j}) and α_{q_j} (α_{c_j}). Every pair of two neighbouring qubits and their middle coupler are coupled through exchange-type interactions with coupling strengths g_{q_j, c_j} , g_{q_{j+1}, c_j}

and $g_{q_j, q_{j+1}}$. Here, the total Hamiltonian has three parts, including qubit-qubit interaction \hat{H}_{Q-Q} , coupler-coupler interaction \hat{H}_{C-C} and qubit-coupler interaction \hat{H}_{Q-C} . The total system is equivalent to a 19-qubit Bose-Hubbard model.

In our experiment, the strong dispersive condition $g_{q_j, c_j} \ll |\Delta_{q_j, c_j}|$ is satisfied, where $\Delta_{q_j, c_j} = \omega_{q_j} - \omega_{c_j}$ is the frequency detuning. By virtue of the so-called Schrieffer-Wolff transformation

$$\hat{U} = \exp \left[\sum_{j=1}^9 \frac{g_{q_j, c_j}}{\Delta_{q_j, c_j}} (\hat{b}_{q_j}^\dagger \hat{b}_{c_j} + \hat{b}_{q_j} \hat{b}_{c_j}^\dagger) + \frac{g_{q_{j+1}, c_j}}{\Delta_{q_{j+1}, c_j}} (\hat{b}_{q_{j+1}}^\dagger \hat{b}_{c_j} + \hat{b}_{q_{j+1}} \hat{b}_{c_j}^\dagger) \right], \quad (\text{S27})$$

one can obtain the effective qubits Hamiltonian

$$\begin{aligned} \hat{H} = \hat{U} \hat{H} \hat{U}^\dagger &= \hat{H}_Q + \hat{H}_{Q-Q} \\ &= \sum_{j=1}^{10} \tilde{\omega}_{q_j} \hat{b}_{q_j}^\dagger \hat{b}_{q_j} + \frac{\alpha_{q_j}}{2} \hat{b}_{q_j}^\dagger \hat{b}_{q_j}^\dagger \hat{b}_{q_j} \hat{b}_{q_j} \\ &\quad + \sum_{j=1}^9 \tilde{g}_{q_j, q_{j+1}} (\hat{b}_{q_j}^\dagger \hat{b}_{q_{j+1}} + \hat{b}_{q_j} \hat{b}_{q_{j+1}}^\dagger). \end{aligned} \quad (\text{S28})$$

with the corresponding dressed frequency

$$\tilde{\omega}_{q_j} = \begin{cases} \omega_{q_j} + \frac{g_{q_j, c_j}^2}{\Delta_{q_j, c_j}}, & j = 1 \\ \omega_{q_j} + \frac{g_{q_j, c_j}^2}{\Delta_{q_j, c_j}} + \frac{g_{q_j, c_{j+1}}^2}{\Delta_{q_j, c_{j+1}}}, & 1 < j < 10 \\ \omega_{q_j} + \frac{g_{q_j, c_{j-1}}^2}{\Delta_{q_j, c_{j-1}}}, & j = 10 \end{cases} \quad (\text{S29})$$

and effective coupling strength

$$\tilde{g}_{q_j, q_{j+1}} = g_{q_j, q_{j+1}} + \frac{g_{q_j, c_j} g_{q_{j+1}, c_j}}{\Lambda_{q_j, q_{j+1}}^{c_j}}, \quad (\text{S30})$$

where $\Lambda_{q_j, q_{j+1}}^{c_j} = 2/(1/\Delta_{q_j, c_j} + 1/\Delta_{q_{j+1}, c_j})$ is the harmonic mean of the frequencies detuning between the j -th coupler and its nearest neighbor qubits. Eq. (S30) implies that the effective qubit-qubit coupling is derived from their direct capacitive coupling and the indirect virtual exchange coupling via the coupler in between. If the frequency of coupler is above the frequencies of qubits, $\Lambda_{q_j, q_{j+1}}^{c_j} < 0$ holds so that the effective coupling $\tilde{g}_{q_j, q_{j+1}}$ can be tuned from positive to negative monotonically with gradually decreasing the frequency of coupler. Experimentally, we use the arbitrary waveform generator (AWG) to generate various fast-bias voltages applied to the corresponding couplers. These pulses on the Z control lines change the frequencies of couplers and then make it possible for the superconducting circuit with tunable couplers to engineer arbitrary coupling distribution.

With $\tilde{g}_{q_j, q_{j+1}} \ll \alpha_{q_j}$, the effective Hamiltonian Eq. (S28) can be rewritten as a site-dependent XY model:

$$\hat{H} = - \sum_{j=1}^9 \kappa_j (\hat{\sigma}_j^+ \hat{\sigma}_{j+1}^- + \hat{\sigma}_j^- \hat{\sigma}_{j+1}^+) - \sum_{j=1}^{10} \mu_j \hat{\sigma}_j^+ \hat{\sigma}_j^-, \quad (\text{S31})$$

where $\hat{\sigma}_j^+$ ($\hat{\sigma}_j^-$) is the raising (lowering) operator of the j -th qubit. Here we choose

$$\kappa_j = -\tilde{g}_{q_j, q_{j+1}}, \quad \mu_j = -\tilde{\omega}_{q_j}. \quad (\text{S32})$$

For the Hamiltonian Eq. (S31), one can map the spin variables to spinless fermion operators by introducing the Jordan-Wigner transformation [40]: $\hat{\sigma}_j^+ = \hat{c}_j^\dagger \exp \left\{ i\pi \sum_{l=1}^{j-1} \hat{c}_l^\dagger \hat{c}_l \right\}$ and $\hat{\sigma}_j^- = \exp \left\{ -i\pi \sum_{l=1}^{j-1} \hat{c}_l^\dagger \hat{c}_l \right\} \hat{c}_j$, where the operators \hat{c}^\dagger and \hat{c}_j satisfy the commutation relations of fermions, i.e., $\{\hat{c}_j, \hat{c}_k\} = \{\hat{c}_j^\dagger, \hat{c}_k^\dagger\} = 0$ and $\{\hat{c}_j, \hat{c}_k^\dagger\} = \delta_{jk}$. Hence, the effective Hamiltonian is mapped into a spinless fermion lattice model as

$$\hat{H} = - \sum_{j=1}^9 \kappa_j (\hat{c}_j^\dagger \hat{c}_{j+1} + \hat{c}_j \hat{c}_{j+1}^\dagger) - \sum_{j=1}^{10} \mu_j \hat{c}_j^\dagger \hat{c}_j. \quad (\text{S33})$$

CORRESPONDENCE WITH TWO-DIMENSIONAL CURVED SPACETIME

Considering the Heisenberg equation $i \frac{d}{dt} \hat{c}_j = [\hat{c}_j, \hat{H}]$, the evolution equation for the operator \hat{c}_j can be given by

$$i \frac{d}{dt} \hat{c}_j = -\kappa_j \hat{c}_{j+1} - \kappa_{j-1} \hat{c}_{j-1} - \mu \hat{c}_j. \quad (\text{S34})$$

By introducing a variable transformation $\tilde{\hat{c}}_j(t) = (-i)^j e^{-i\mu t} \hat{c}_j$, we obtain

$$\frac{d}{dt} \tilde{\hat{c}}_j(t) = -\kappa_j \tilde{\hat{c}}_{j+1}(t) + \kappa_{j-1} \tilde{\hat{c}}_{j-1}(t). \quad (\text{S35})$$

Here $\tilde{\hat{c}}_j(t)$ can be viewed as a quantized operator of a discrete field $\varphi_j(t)$, where d denotes the lattice constant and the spatial position can be discretized as $x = x_j = x_h + jd$ with $x_h = j_h d$ and $j \in \mathbb{Z}^+$. Now let us recover the continuous field $\varphi(t, x)$. If we define a function f that is dependent of the spatial position x_j and substitute κ_j as,

$$\kappa_j = \frac{f(x_{j+1}) + f(x_j)}{8d}, \quad (\text{S36})$$

according to Eq. (S35), $\varphi(t, x_j) \rightarrow \tilde{\hat{c}}_j(t)/\sqrt{d}$ will obey the following relation in the continuum limit,

$$\begin{aligned}
\frac{\partial}{\partial t} \varphi(t, x) &= -\frac{f(x_{j+1}) + f(x_j)}{8d} \varphi(t, x_{j+1}) + \frac{f(x_j) + f(x_{j-1})}{8d} \varphi(t, x_{j-1}) \\
&= -\frac{f(x_j)}{4} \cdot \frac{\varphi(t, x_{j+1}) - \varphi(t, x_{j-1})}{2d} - \frac{1}{4} \cdot \frac{f(x_{j+1})\varphi(t, x_{j+1}) - f(x_{j-1})\varphi(t, x_{j-1})}{2d} \\
&= -\frac{f(x)}{4} \cdot \frac{\partial}{\partial x} \varphi(t, x) - \frac{1}{4} \cdot \frac{\partial}{\partial x} [f(x)\varphi(t, x)] \\
&= -\frac{f(x)}{2} \cdot \frac{\partial}{\partial x} \varphi(t, x) - \frac{f'(x)}{4} \varphi(t, x).
\end{aligned} \tag{S37}$$

In fact, Eq. (S37) can be considered as a special case of Dirac equation in the massless limit $m \rightarrow 0$ if we decompose the Dirac field operator into $\psi = \frac{1}{\sqrt{2}}(\xi + \varphi, \xi - \varphi)^T$. In the light of Refs [24, 41], the Dirac equation in (1+1)-dimensional curved spacetime with the metric $g_{\mu\nu}$ is written as

$$i\gamma^a e_{(a)}^\mu \partial_\mu \psi + \frac{i}{2} \gamma^a \frac{1}{\sqrt{-g}} \partial_\mu (\sqrt{-g} e_{(a)}^\mu) \psi - m\psi = 0, \tag{S38}$$

where the dyad $e_{(a)}^\mu$ satisfies the orthonormal condition $e_{(a)}^\mu e_{(a)}^\nu = \delta_\mu^\nu$ and the γ -matrices in the two-dimensional case are $\gamma^0 = \sigma_z$ and $\gamma^1 = i\sigma_y$. When the dyad is chosen as

$$e_{(a)}^\mu = \begin{pmatrix} -1 & 1 \\ \frac{1-f}{2} & \frac{1+f}{2} \end{pmatrix}. \tag{S39}$$

Thus, Eq. (S38) can be decomposed into two independent equations,

$$\partial_t \varphi = -\frac{f}{2} \partial_x \varphi - \frac{f'}{4} \varphi + \frac{i}{2} m \xi, \quad \partial_x \xi = -im\varphi. \tag{S40}$$

In the massless limit $m \rightarrow 0$, one can find that Eq. (S40) is in accord with Eq. (S37). Hence, what the effective Hamiltonian Eq. (S33) describes is equivalent to a two-dimensional static curved spacetime governed by the massless Dirac equation if we set κ_j as

$$\kappa_j = \frac{f(x_{j+1}) + f(x_j)}{8d} \approx \frac{f(x_j + d/2)}{4d}. \tag{S41}$$

There is only one single nondegenerate horizon x_h so that $f(x_h) = 0$ and $f(x) > 0$ when $x > x_h$ and

$$g_h = \frac{1}{2} f'(x_h) > 0, \tag{S42}$$

where g_h is the surface gravity of the horizon, which gives the Hawking temperature $T_H = g_h/(2\pi)$. In the main text, we set $f(x) = \beta \tanh x$ with corresponding Hawking temperature $T_H = \beta/(4\pi)$ and

$$\kappa_j = \frac{\beta \tanh((j - j_h + 1/2)d)}{4d}. \tag{S43}$$

What we have shown above is the correspondence between XY model and the (1+1)-D Dirac field. The case of scalar field governed by Klein-Gordon equation is similar. For a complete presentation, one can refer to the earlier theoretical work [18]. Here we briefly summarize the theoretical framework, as shown in Fig. S3.

EXPERIMENTAL SETUP AND DEVICE PARAMETERS

Our superconducting quantum processor is placed in a BlueFors dilution refrigerator. The base temperature of mixing chamber (MC) is about 9 mK. All qubits share one readout line equipped with a Josephson parametric amplifier (JPA) and a high-electron-mobility transistors (HEMT). Pulse on the readout transmission line is first generated as a mixture of local oscillation (LO) and the envelopes from an arbitrary waveform generator (AWG) and then demodulated by an analog digital converter (ADC). In this experiment, we replace the DC bias with a long Z square pulse generated by AWGs. Both XY and Z control signals are programmed in advance before being uploaded to AWGs. A schematic diagram of experiment setup is given in Fig. S4.

The device parameters are briefly shown in Table S1. All the parameters are characterized by various relatively efficient and automatic methods, especially the parameters concerning couplers. Details of those methods in our experiment will be introduced in the following.

EFFICIENT AND AUTOMATIC CALIBRATION FOR MULTI-QUBIT DEVICES WITH TUNABLE COUPLERS

Before carrying out our experiment for simulating an analogue black hole, we need calibrate all 10 qubits and find the useful parameters of 9 couplers. This is far more difficult and time-consuming than calibrating a typical 10-qubit sample without tunable couplers. In order to measure and characterize device parameters more efficiently, we adopt an automatic calibration technology based on a combination of physical models and optimization methods.

Spectrum of qubit and frequency calibration

First and foremost, all the qubits are individually brought up through the standard single-qubit calibration (from identifying the readout resonator frequency to calibrating π pulse). If a qubit is brought up at a certain fre-

qubit	Q_1	Q_2	Q_3	Q_4	Q_5	Q_6	Q_7	Q_8	Q_9	Q_{10}
$\tilde{\omega}_{q_j}^{01}/2\pi$ (GHz)	5.300	4.760	5.330	4.805	5.278	4.830	5.231	4.705	5.180	4.655
$\tilde{\omega}_{q_j}^r/2\pi$ (GHz)	6.667	6.687	6.708	6.733	6.749	6.772	6.792	6.815	6.840	6.857
$E_C/2\pi$ (MHz)	195.8	194.5	195.4	198.4	197.0	196.2	195.7	201.8	199.7	203.2
$E_{JJ}/2\pi$ (GHz)	20.69	19.88	19.78	18.55	19.30	19.52	19.39	17.66	18.64	18.00
F_{0,q_j}	0.965	0.958	0.974	0.938	0.956	0.940	0.982	0.952	0.949	0.943
F_{1,q_j}	0.885	0.901	0.907	0.887	0.885	0.910	0.871	0.875	0.904	0.906
T_{1,q_j} (μ s)	24.9	20.1	18.6	27.8	27.9	25.4	24.1	23.5	37.4	27.7
$T_{2,q_j}^*/(\mu$ s)	4.2	1.5	5.4	2.0	5.9	1.9	5.2	2.7	5.9	2.0
$T_{2,q_j}^{\text{Echo}}/(\mu$ s)	7.2	3.4	17.9	4.4	10.7	4.6	11.3	5.3	9.0	4.1
coupler	C_1	C_2	C_3	C_4	C_5	C_6	C_7	C_8	C_9	
$g_{q_j,c_j}/2\pi$ (MHz)	98.07	84.13	98.88	85.96	96.46	87.50	96.00	85.63	96.02	
$g_{q_{j+1},c_j}/2\pi$ (MHz)	85.72	96.68	88.64	97.46	85.36	96.78	85.89	97.40	83.36	
$g_{q_j,q_{j+1}}/2\pi$ (MHz)	10.41	10.06	10.05	9.73	9.56	9.97	9.55	9.64	9.82	

TABLE S1. List of device parameters. Here, $\tilde{\omega}_{q_j(c_j)}^{01}$ is $|0\rangle \rightarrow |1\rangle$ transition frequency of the j -th qubit (coupler) with the corresponding readout frequency $\tilde{\omega}_{q_j}^r$. E_C and E_{JJ} denote the charging energy and the Josephson energy. F_{0,q_j} and F_{1,q_j} are measure fidelities of $|0\rangle$ and $|1\rangle$, respectively. T_{1,q_j} represents the energy relaxation time of q_j at the idle point. The dephasing time T_{2,q_j}^* is characterized by the Ramsey fringe experiment, while T_{2,q_j}^{Echo} is measured by spin echo sequence with an inserted π pulse. The coupling strengths of exchange-type interactions between qubits and the corresponding coupler are g_{q_j,c_j} and g_{q_{j+1},c_j} , and the direct coupling of qubits is $g_{q_j,q_{j+1}}$.

quency, we need perform a two-dimensional spectroscopy measurement to extract the mapping between Z-pulse amplitude (hereinafter referred as Zpa, each unit of 200 mV) of qubit bias and its frequency (such as Fig. S5) and this will contribute to automatically calibrate all the qubits together.

According to our all-transmon sample, each transmon consists of two parallel SIS-type Josephson junctions connected by a loop which is in series with a capacitor. The critical currents of two junctions are I_{c_1} and I_{c_2} and E_C denotes the charging energy of capacitor. By using the perturbation theory, the transition frequency can be approximately written as [42–44]

$$\omega(\Phi) \approx \sqrt{8E_{JJ}E_C \sqrt{\delta^2 + \cos^2\left(\frac{\pi\Phi}{\Phi_0}\right)}} - E_C, \quad (\text{S44})$$

where $\Phi_0 = h/(2e)$ is the unit flux, $E_{JJ} = \sqrt{I_{c_1}I_{c_2}}\Phi_0/\pi$ denotes the geometric mean of two junctions energy in the zero field and $\delta = |I_{c_1} - I_{c_2}|/(2\sqrt{I_{c_1}I_{c_2}})$ represents the junction asymmetry. Here, the total magnetic flux Φ is in direct proportion with the strength of the magnetic field threading the loop and this weak magnetic field induced by Z pulse is approximately proportional to Zpa ($\Phi \propto \text{Zpa}$). Thus, the mapping between qubit Zpa and its frequency can be given by

$$\omega(\text{Zpa}) \approx \sqrt{8E_{JJ}E_C \sqrt{\delta^2 + \cos^2(A \cdot \text{Zpa} + \phi)}} - E_C \quad (\text{S45})$$

and

$$\text{Zpa}(\omega) \approx \frac{\arccos\left[\pm\sqrt{\frac{(\omega+E_C)^4}{(8E_{JJ}E_C)^2} - \delta^2}\right] - \phi}{A}, \quad (\text{S46})$$

where E_C can be measured by two-photon excitation experiment (double difference between two-photon excitation frequency and qubit frequency), the remaining parameters E_{JJ} , δ , A and ϕ will be obtained by fitting the two-dimensional spectrum of qubits. Here parameter A describes the efficiency of qubit bias which depends on the attenuation on the Z control line, while ϕ is the initial flux shift. Even if the refrigerator temperature rises and cools again, only ϕ may have some displacement. As long as the circuit wiring does not change, parameter A will keep its value. Notice, however, that Eq. (S45) and Eq. (S46) need to be modified by the crosstalk of Z control lines if multi-qubit case is involved.

When we design the multi-qubit levels, Eq. (S46) will be beneficial to obtain the corresponding Zpa according to the target frequency. A more accurate frequency calibration can be implemented by Ramsey fringe experiment.

Calibration of pulse distortion and Z crosstalk

Although the Z pulse generated by AWG is designed carefully, the shape of the pulse is distorted when it interacts with the qubit. To calibrate the distortion of step

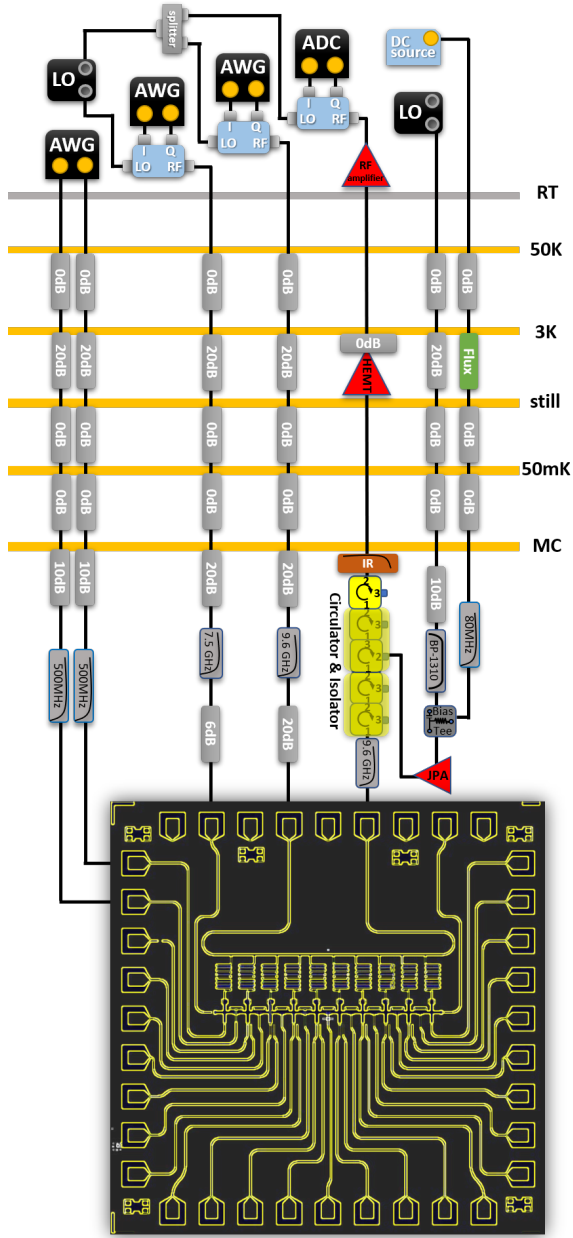


FIG. S4. A schematic diagram of the experimental system and partial wiring information.

response, we use several first-order infinite impulse response (IIR) filters and a finite impulse response (FIR) filter [45]. Here IIR filters are designed to be an integration of several exponential functions and FIR filter is described by a polynomial with 20 parameters. The results of pre- and post-correction are shown in Fig. S6.

For the crosstalk of Z control lines between qubits and qubits or qubits and their non-nearest neighbor couplers, a routine Z crosstalk measurement with a small scanning range is adopted, which can be used to estimate the crosstalk coefficients by measuring the frequency re-

sponse to the Z control lines. However, it may be better to extend to a wider range of scanning when it comes to the Z crosstalk of couplers to qubits. If the frequency of coupler approaches the frequency of qubit, the effect of anti-crossing will be amplified due to the strong coupling between coupler and its nearest neighbor qubit, leading to a distinctly non-linear relationship between coupler Z_{pa} and qubit Z_{pa} (as shown in Fig. S7b). To correct the crosstalk from classical flux crosstalk of Z control lines that basically meet the linear relationship, we first select a range of data away from the resonance points to use linear fitting, and constantly fine-tune the corresponding crosstalk coefficient until a symmetrical anti-crossing pattern is obtained. For a more accurate Z crosstalk calibration, we still take advantages of Ramsey fringe experiment, but proximity to the resonance points should be avoided. Here we emphasize that in our procedure of calibration, Z crosstalk of couplers to qubits must be corrected in order to more accurately measure spectrum of coupler and coupling strengths, as explained in the following.

Spectrum of coupler and anti-crossing of energy levels

As what mentioned above, it is difficult to directly excite and measure a coupler because it has no XY control line and readout resonator. Therefore, we make use of two qubits (Q_j and Q_{j+1}) that are adjacent to the cou-

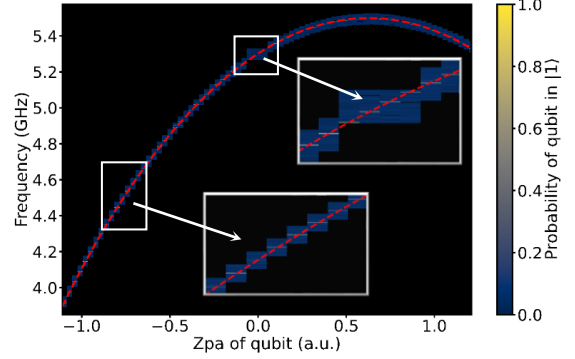


FIG. S5. Experimental data of qubit automatical spectroscopy measurement. Here we take the spectrum of Q_1 as an example. The black area is unscanned in order to save time. We first scan a small square area (about four columns data) around $Z_{pa} = 0$ and then use polynomial curves to fit the peaks of these data. The corresponding polynomial fitting coefficients will help predict the next peak of qubit spectrum. By constantly measuring, fitting and predicting, we obtain the experimental data of qubit spectrum with a wide range. The mapping between qubit Z_{pa} and its frequency can be obtained by fitting the experimental data based on Eq. (S45).

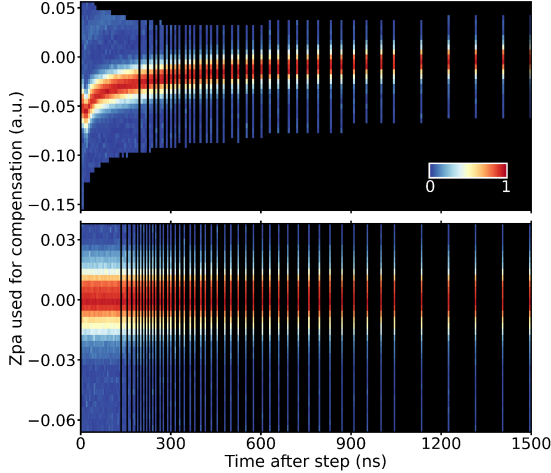


FIG. S6. Experimental data of pulse shape measurement. The black area is unscanned in order to save time. Here the heatmap denotes the probability of qubit in $|1\rangle$. The uncorrected pulse (up) is distorted, while the corrected result (down) shows a stationary step response.

pler (C_j) to perform a coupler spectroscopy measurement (after the calibration of Z crosstalk). To be specific, we apply XY excitation pulse to one of the qubits (Q_j) and vary the Zpa of coupler. If the coupler is excited to $|1\rangle$ by the crosstalk from Q_j XY line, the frequency of another qubit (Q_{j+1}) will be changed due to the AC Stark effect between them. At the moment, a π pulse calibrated before is unable to cause the perfect transition of Q_{j+1} due to its variation of frequency and its population of excited state will be decreased [20, 21] (see pulse sequence in the inset of Fig. S8a). In this way, one can obtain the spectrum of the local $Q_j C_j Q_{j+1}$ three-body system, which are actually the first three eigen-spectra (red lines in Fig. S8a) of the three-body Hamiltonian [19, 21]

$$\hat{H}_{Q_j C_j Q_{j+1}} = \sum_k \omega_k \hat{b}_k^\dagger \hat{b}_k + \frac{\alpha_k}{2} \hat{b}_k^\dagger \hat{b}_k^\dagger \hat{b}_k \hat{b}_k + \sum_{k \neq l} g_{k,l} (\hat{b}_k^\dagger \hat{b}_l + \hat{b}_k \hat{b}_l^\dagger) \quad (\text{S47})$$

with $k \in \{q_j, c_j, q_{j+1}\}$. In Eq. (S47), the qubits frequencies ω_{q_j} and $\omega_{q_{j+1}}$ are fixed and all anharmonicities $\alpha = -E_C$ can be obtained by two-photon excitation measurement. Furthermore, the coupling between qubit and coupler is much stronger than $g_{q_j, q_{j+1}}$ in our device. Thus, there leaves 5 parameters to be determined in this three-body Hamiltonian, namely 2 coupling strengths (i.e., g_{q_j, c_j} and $g_{q_j, c_{j+1}}$) and 3 parameters of ω_{c_j} (i.e., E_{JJ} , A , ϕ in Eq. (S45)).

Note that the smallest gaps of the two anti-crossing spectral lines represent twice the coupling strengths, respectively. However, it is inaccurate to estimate the coupling strengths only by scanning the three-body spectrum due to the broadening of spectral lines and some

impure peaks [46, 47]. For more accurate measurement, we scan two extra anti-crossing spectrums of two-body systems $Q_j C_j$ and $Q_{j+1} C_j$, as shown in Fig. S8b. Truncated to two energy levels, the Hamiltonian of a qubit Q_j coupled to a coupler C_j can be expressed in the subspace basis $\{|10\rangle, |01\rangle\}$ as

$$\hat{H}_{Q_j C_j} = \begin{pmatrix} \omega_{q_j} & g_{q_j, c_j} \\ g_{q_j, c_j} & \omega_{c_j} \end{pmatrix}, \quad (\text{S48})$$

and its eigen-energy spectra are

$$\omega_{Q_j C_j}^\pm = \frac{\omega_{q_j} + \omega_{c_j}}{2} \pm \sqrt{\frac{g_{q_j, c_j}^2}{4} + \frac{(\omega_{q_j} - \omega_{c_j})^2}{4}}. \quad (\text{S49})$$

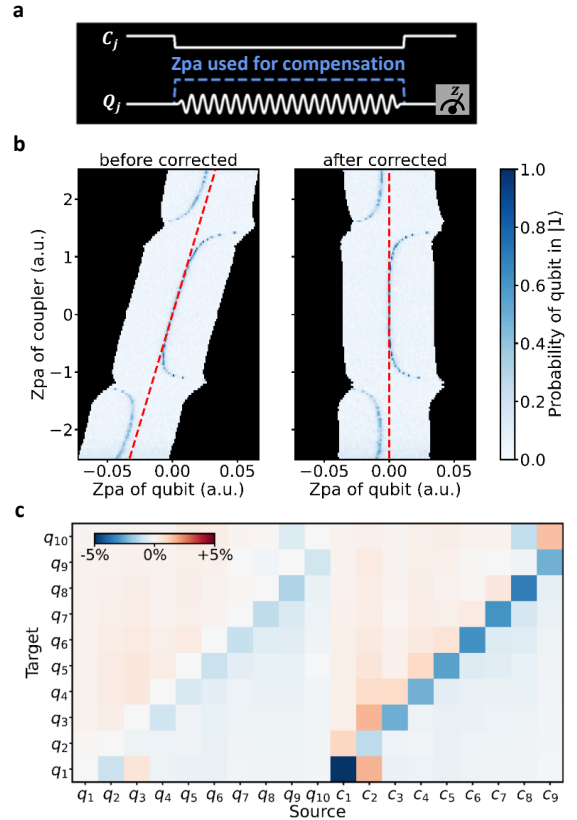


FIG. S7. Experimental data of automatical Z crosstalk calibration. **a**, Pulse sequence for measurement of Z crosstalk of coupler to qubit. **b**, Before Z crosstalk is corrected, one can observe a tilted anti-crossing pattern of qubit and its nearest neighbor coupler. By constantly fine-tuning the crosstalk coefficient and applying the Zpa to compensate crosstalk from coupler Z line, a symmetrical anti-crossing pattern will be obtained after corrected. The black area is unscanned, while the red lines are the results of linear fitting. Here we show the experimental data of Z crosstalk calibration **c**, All the coefficients of Z crosstalk. Compared with the high crosstalk from couplers Z line to qubits, the absolute coefficients of Z crosstalk between qubits are all at a low level ($< 2\%$).

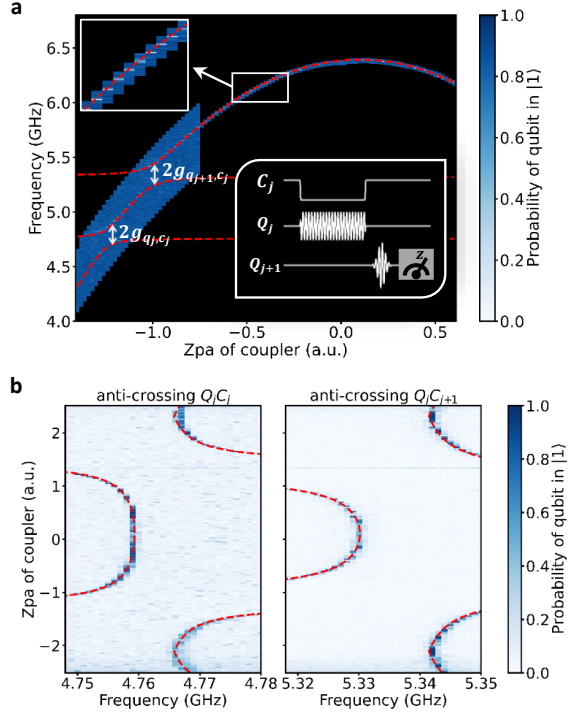


FIG. S8. Experimental data of coupler automatical spectroscopy measurement. The red curves are numerical simulation results for fitting the peaks of spectroscopy data, which is based on a multi-objective optimization. **a**, The spectrum of the local $Q_j C_j Q_{j+1}$ three-body system. The black area is unscanned, while the experimental data consists of the blue area. When the frequency of coupler is far from the qubits frequency, we only need to scan a very narrow width like single-qubit spectroscopy measurement. As it approaches the anti-crossing points, we increase the scan width to reduce the impact caused by predictive error, which ensures a clear three-body spectrum and saves time simultaneously. **b**, Experimental data of anti-crossing spectrums of $Q_j C_j$ (left) and $Q_{j+1} C_j$ (right). Here the results of C_2 are taken as an example.

Similarly, the eigen-energy spectra of $Q_{j+1} C_j$ are

$$\omega_{Q_{j+1} C_j}^{\pm} = \frac{\omega_{q_{j+1}} + \omega_{c_j}}{2} \pm \sqrt{g_{q_{j+1}, c_j}^2 + \frac{(\omega_{q_{j+1}} - \omega_{c_j})^2}{4}}. \quad (\text{S50})$$

Combining the above two equations with the diagonalization result of Eq. (S47), one can finally determine the coupling strengths between coupler and qubits (i.e., g_{q_j, c_j} and g_{q_{j+1}, c_j}) and the mapping between coupler frequency ω_{c_j} and its Zpa. Actually, this is a multi-objective optimization problem of simultaneously fitting 3 spectroscopy results via 5 parameters. We utilize the optimization function `scipy.optimize.minimize` in the Python module SciPy to solve this problem.

Measurement of the effective coupling

To measure the effective coupling strength $\tilde{g}_{q_j, q_{j+1}}$, we measure the joint probability as a function of qubit-qubit swapping time t and the Zpa of coupler [46, 47], as shown in Fig. S9b. Similar to Eq. (S48), the swapping Hamiltonian of $Q_j Q_{j+1}$ in the subspace effective basis $\{|\widetilde{10}\rangle, |\widetilde{01}\rangle\}$ is

$$\hat{H}_{Q_j Q_{j+1}} = \begin{pmatrix} \tilde{\omega}_{q_j} & \tilde{g}_{q_j, q_{j+1}} \\ \tilde{g}_{q_j, q_{j+1}} & \tilde{\omega}_{q_{j+1}} \end{pmatrix}. \quad (\text{S51})$$

If $Q_j Q_{j+1}$ is initially in state $|\widetilde{01}\rangle$, the time-dependent joint probability $P_{01}(t) = \langle \widetilde{01} | e^{-i\hat{H}_{Q_j Q_{j+1}} t} | \widetilde{01} \rangle$ can be expressed as

$$P_{01}(t) = \frac{1}{2} \cos \left[\sqrt{4\tilde{g}_{q_j, q_{j+1}}^2 + (\tilde{\omega}_{q_j} - \tilde{\omega}_{q_{j+1}})^2} t \right] + \frac{1}{2}, \quad (\text{S52})$$

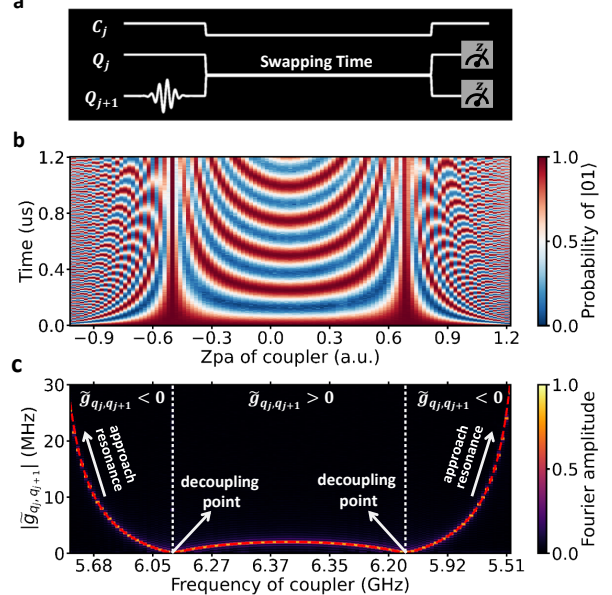


FIG. S9. Experimental data of the effective coupling strength measurement. **a**, Pulse sequence for measurement of swapping between qubits while changing the Zpa of coupler. **b**, Measured joint probability P_{01} of qubits vs Zpa of coupler (or corresponding frequency) and the swapping time. **c**, The Fourier transform of **b**, where the heatmap represents the normalized Fourier amplitude. The relation between absolute effective coupling strength $|\tilde{g}_{q_j, q_{j+1}}|$ and coupler Zpa (or corresponding frequency) is given by each peak of normalized Fourier amplitude. The red dash line is the fitting curve of $|\tilde{g}_{q_j, q_{j+1}}|$ by using Eq. (S54), while white dot lines denote two decoupling points ($\tilde{g}_{q_j, q_{j+1}} = 0$). As coupler frequency decreases, $|\tilde{g}_{q_j, q_{j+1}}|$ decreases from positive to zero. Once it passes the decoupling point, $|\tilde{g}_{q_j, q_{j+1}}|$ becomes negative and its absolute value will increase rapidly, in especial approach to resonance point of qubits.

which is reduced to

$$P_{01}(t) = \frac{1}{2} \cos(2\tilde{g}_{q_j, q_{j+1}} t) + \frac{1}{2} \quad (\text{S53})$$

when the two qubits are resonant, namely $\tilde{\omega}_{q_j} = \tilde{\omega}_{q_{j+1}}$. Thus, the effective coupling strength can be calculated as half the Fourier frequency of probability $P_{01}(t)$. It needs to be emphasized that decoherence may cause the damping amplitude of swapping probability but does not affect the Fourier frequency.

For each Zpa of coupler (related to its frequency), we calculate $\tilde{g}_{q_j, q_{j+1}}$ via measuring $P_{01}(t)$ and performing Fourier transform (as shown in Fig. S9c). Subsequently,

one can utilize Eq. (S30) to draw the mapping between the effective coupling strength and coupler Zpa:

$$\tilde{g}_{q_j, q_{j+1}}(\text{Zpa}) = g_{q_j, q_{j+1}} + \frac{g_{q_j, c_j} g_{q_{j+1}, c_j}}{\omega_{c_j}(\text{Zpa}) - \omega}, \quad (\text{S54})$$

where $\omega = \omega_{q_j} = \omega_{q_{j+1}}$ is the resonant frequency of qubits, the direct coupling $g_{q_j, q_{j+1}}$ is the fitted value and the coupler frequency $\omega_{c_j}(\text{Zpa})$ obeys Eq. (S45). Hence, if the Zpa of coupler is given, the effective coupling strength can be computed via Eq. (S54); or given a target coupling, one can estimate the Zpa of coupler by

$$\text{Zpa}(\tilde{g}_{q_j, q_{j+1}}) \approx \frac{1}{A} \arccos \left[\pm \frac{1}{8E_{\text{JJ}}E_{\text{C}}} \sqrt{\left(\omega + E_{\text{C}} + \frac{g_{q_j, c_j} g_{q_{j+1}, c_j}}{\tilde{g}_{q_j, q_{j+1}} - g_{q_j, q_{j+1}}} \right)^2 - \left(8E_{\text{JJ}}E_{\text{C}}\delta \right)^2} \right] - \frac{\phi}{A}, \quad (\text{S55})$$

where E_{JJ} and E_{C} are the Josephson energy and the charging energy of coupler, respectively. Eq. (S55) is a crucial foundation for engineering arbitrary coupling distribution in a superconducting circuit with tunable couplers.

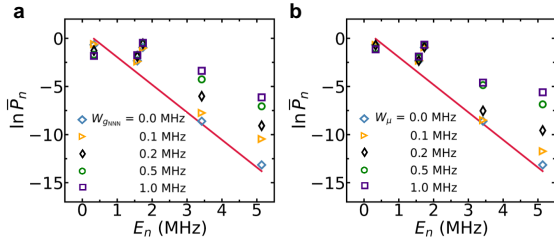


FIG. S10. The effects of two typical disorders on Hawking radiation. **a**, The logarithm of average radiation probability vs. the positive energy of particle with different disorder strengths of g_{NNN} . **b**, The logarithm of average radiation probability vs. the positive energy of particle with different disorder strengths of μ . Here, the red solid line represents the theoretical result.

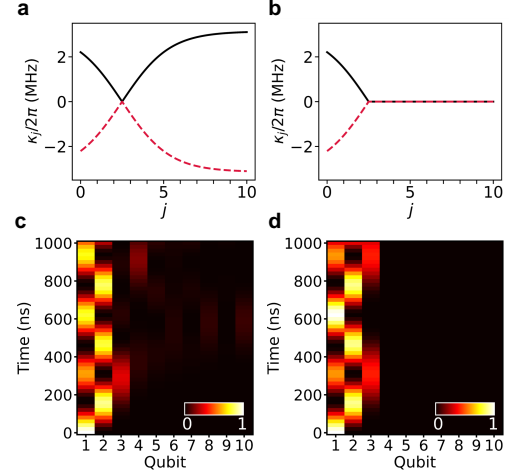


FIG. S11. Quantum walks of different coupling distribution. **a**, The couplings keep the same amplitude inside and outside of the black hole, where the black solid line represents all couplings keeping positive and the red dash line denotes all couplings remaining negative. These two cases are equivalent and the same results are shown in **c**. **b**, Non-zero coupling inside the black holes (black solid line and red dash line imply positive coupling and negative coupling respectively) and zero coupling between all sites outside the black hole, where the corresponding results of quantum walks are shown in **d**. Here we take the initial state $|1000000000\rangle$ as an example.

ADDITIONAL DISCUSSION

For further discussion, we perform additional numerical simulations to compare and supplement with our results in this paper. In the following, the effects of disorders, different coupling distribution and finite size are investigated.

The effects of disorders

In reality, qubits are doomed to be disturbed by various disorders, leading to the nuance between experimental conditions and theoretical assumptions. For a 1D-array of qubits, one can consider two disorders about next-nearest-neighbor (NNN) coupling g_{NNN} and on-site

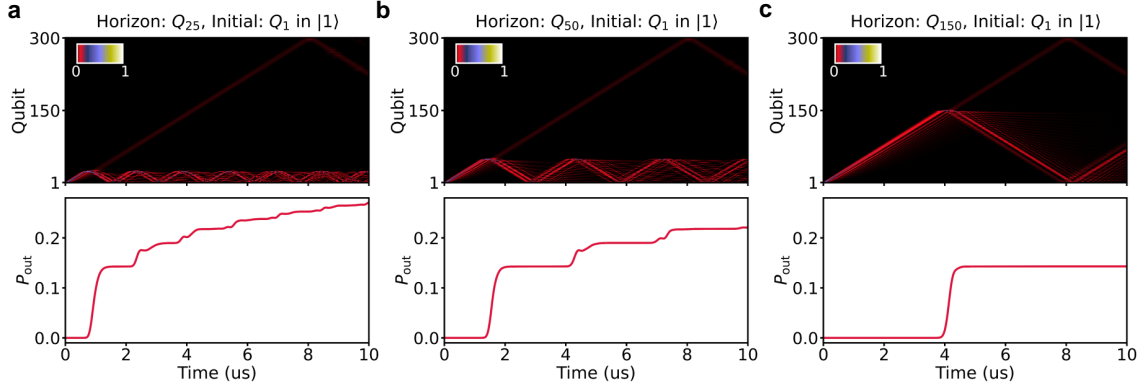


FIG. S12. Simulation of a 300-qubit chain with horizons at different locations. Here the coupling κ_j takes the form of Eq. (S43), where $d = 0.35$ and $\beta/(2\pi) = 4.39$ MHz. From **a** to **c**, the corresponding horizons are located at Q_{25} , Q_{50} and Q_{150} , respectively. P_{out} is defined as the sum of probabilities of all the qubits outside the horizon.

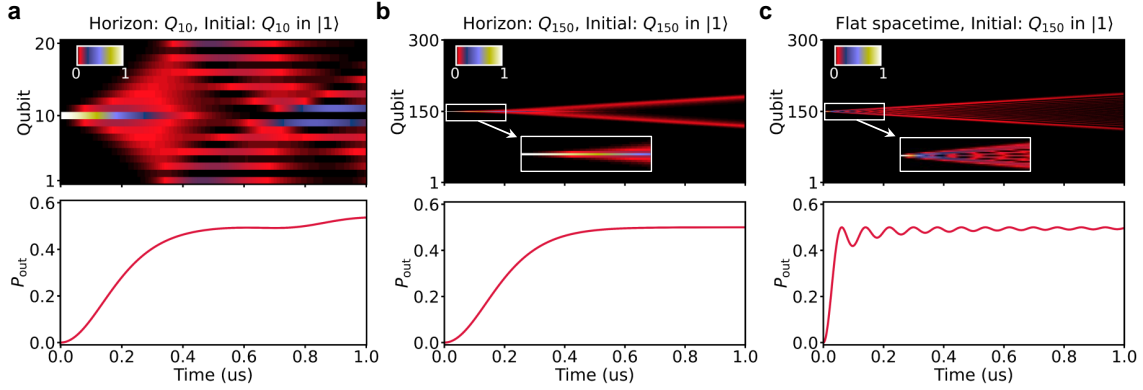


FIG. S13. The finite-size effects on the horizon. The particle is initialized at the horizon. **a**, Simulation of a 20-qubit chain with the horizon located at Q_{10} . **b**, Simulation of a 300-qubit chain with the horizon located at Q_{150} . Here the coupling κ_j takes the form of Eq. (S43), where $d = 0.35$ and $\beta/(2\pi) = 4.39$ MHz. **c**, Simulation of a 300-qubit chain in flat spacetime with $\kappa_j = 3.14$ MHz. P_{out} is defined as the sum of probabilities of all the qubits outside the horizon.

potential μ with the corresponding disorder strengths $W_{g_{\text{NNN}}}$ and W_μ . Specifically, the Hamiltonian of disorders is

$$\hat{H}_{\text{dis}} = \sum_{j=1}^8 g_{\text{NNN}}^j (\hat{\sigma}_j^+ \hat{\sigma}_{j+2}^- + \hat{\sigma}_j^- \hat{\sigma}_{j+2}^+) - \sum_{j=1}^{10} \mu_j \hat{\sigma}_j^+ \hat{\sigma}_j^-, \quad (\text{S56})$$

where the site-dependent g_{NNN}^j and μ_j are in $[-W_{g_{\text{NNN}}}, W_{g_{\text{NNN}}}]$ and $[-W_\mu, W_\mu]$, and their distribution are assumed to be uniform. To probe the effects of disorders, we numerically model the dynamics of Hawking radiation by considering \hat{H}_{dis} . In Fig. S10a and b, one can note that both disorders diverge the probability spectrum and theoretical results of Hawking radiation, especially in the condition of strong disorder. However, we measure the NNN coupling of $g_{\text{NNN}}^j \approx 0.1$ MHz and the frequencies difference of $|\mu_j - \omega_{\text{ref}}| < 0.2$ MHz with reference frequency $\omega_{\text{ref}}/(2\pi) \approx 5.1$ GHz. According to Fig. S10, such small degree of disorders have little im-

pact on the results of Hawking radiation in experiment. In fact, we measure the initial density matrix of 7 qubits outside the horizon. The fidelity between the imperfect initial state in experiment and ideal initial state is 99.2% (see Fig. 3a in the main text), which may be caused by the XY crosstalk, thermal excitation, leakage, etc. We substitute such an experimental state for the ideal initial state in the numerical simulation of Hawking radiation, then the results of numerical simulation agree with experimental results better (see Fig. 3d in the main text).

Different coupling distribution

Admittedly, our model does not mandate flipping the sign of coupling κ_j near the horizon. In the main text, we request that the coupling goes monotonically from negative to positive (or vice versa) from the left of horizon to

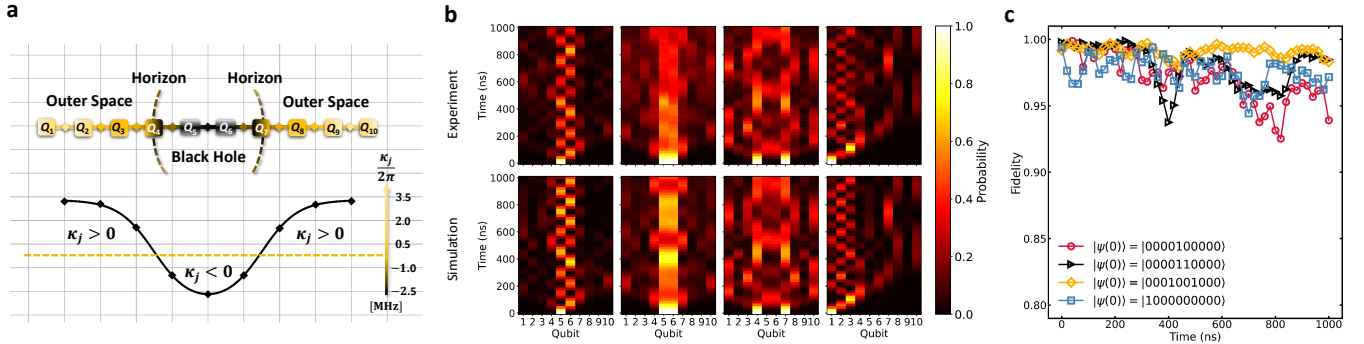


FIG. S14. Quantum walks in a 1D array of 10 superconducting qubits with black hole at the center. **a**, Schematic representation of the black hole at the center and the corresponding coupling distribution. **b**, Quantum walks in such a curved spacetime. The heatmap denotes the probabilities of excited-state for Q_i in time. The horizontal axis is indexed as qubit number i , the vertical axis is time. Here we show both the numerical simulation and experiment data. **c**, Fidelity of the experimental data compared to ideal numerical simulation of quantum walks.

its right side. This is based on the realistic consideration of the smoothness of $f(x)$. In fact, if instead of flipping the sign of couplings they were all kept positive (or negative) inside and outside of the black hole (Fig. S11a), all of the results would be similar, as shown in Fig. S11c. For the case with non-zero coupling inside the black hole but zero coupling between all sites outside the black hole (Fig. S11b), one can find the results inside black hole are also similar with the results in case of flipping the sign of couplings, but it is quite different for the results outside black hole. Due to the zero coupling between all sites outside, no particles can travel in the exterior (Fig. S11d) and thus no radiation can be detected by the observer outside.

The finite-size effects

Here we perform the numerical simulation of a 300-qubit chain to show the finite-size effects more clearly when we initialize the system by preparing a particle in the black hole. When the particle arrives at the horizon, it is going to be reflected back into the black hole in all probability but has a little chance to appear in the outside. The horizon is similar to a ‘membrane’ with certain transmittance, see Fig. S12. The probability of finding the particle outside P_{out} shows a general upward trend due to the Hawking radiation. However, the particle will be reflected when it arrives at the boundary (Q_1 or Q_{300}) due to the finite-size effects. When the particle reflected by the boundary of the black hole reaches the horizon again, it has a certain probability to escape into the outside and P_{out} thus increases again (see Fig. S12a and Fig. S12b). Conceivably, if there are no boundaries,

P_{out} will be increase to a certain value and eventually the particle reaches a steady state of radiation.

In addition, the finite size can also affect the horizon. In the continuous curved spacetime, the particle initialized at the horizon is bound to the horizon forever due to the zero couplings on both sides of the horizon. However, in the finite-size lattice, the coupling strengths on both sides of the horizon are not strictly zero even though they are very small. As shown in Fig. S13a and Fig. S13b (also Fig. 2b in the main text), although the particle seems to be localized at the horizon for a very short time, it is doomed to escape from the constraints. When the particle is far from the horizon, its behavior is similar to that in flat spacetime (see Fig. S13b and Fig. S13c).

EXTENDED DATA

In addition, we design an analogue black hole at the center of our 1D array superconducting qubits, see Fig. S14a. Here the coupling κ_j is designed as $\beta(\tanh((j - 7/2)d) - \tanh((j - 13/2)d) + 1)/(4d)$ with $d = 1$ a.u. and $\beta/(2\pi) \approx 13.2$ MHz. The qubits Q_5 and Q_6 are in the interior of the black hole, Q_4 and Q_7 are at the horizon, and other qubits are in the outer space. In Fig. S14b, we prepare four initial states to show quantum walks in such a curved spacetime, i.e., $|0000100000\rangle$, $|0000110000\rangle$, $|0001001000\rangle$ and $|1000000000\rangle$, respectively. The results of quantum walks of black hole at the center in the chain are similar to the results of black hole at the leftmost boundary in the main text. However when the black hole is at the center, finite size effect in the experimental 10-qubit 1D array becomes obvious, for which the tunneling out particle soon reaches the boundary and is reflected back.